Multifunctional Er^{3+}-Doped SrBi$_2$Ta$_2$O$_9$ Ceramics: Optimized Energy Storage and Photoluminescence Properties for Advanced Electronic Applications

A DISSERTATION

SUBMITTED IN PARTIAL FULFILLMENT OF THE REQUIREMENTS FOR THE AWARD OF THE DEGREE

OF

MASTER OF SCIENCE

IN

PHYSICS

Submitted by:

VYOM KHARE   **DEVESH GARG**

(23/MSCPHY/60)   **(23/MSCPHY/18)**

Under the supervision of

Dr.Renuka Bokolia

(Assistant Professor)

DEPARTMENT OF APPLIED PHYSICS

DELHI TECHNOLOGICAL UNIVERSITY

(Formerly Delhi College of Engineering)

Bawana Road, Delhi-110042

JUNE, 2025

Candidate's declaration

We, **Vyom Khare**, Roll No. **23/MSCPHY/60** and **Devesh Garg**, Roll No. **23/MSCPHY/18** students of M.Sc. Physics here by declare that the project Dissertation titled "**SUBMITTED IN PARTIAL FULFILLMENT OF THE REQUIREMENTS FOR THE AWARD OF THE DEGREE** "which is submitted by us to the Department of Applied Physics, Delhi Technological University, Delhi in partial fulfilment of the requirement for the award of the degree of Master of Science, is original and not copied from any source without proper citation. This work has not previously formed the basis for the award of any Degree, Diploma Associateship, Fellowship or other similar title or recognition.

The work has been accepted in peer-reviewed Scopus indexed conference with the following details:

Title of Paper: "Structural and Photoluminescence Properties of Er^{+3} Doped $SrBi_2Ta_2O_9$ Ceramics"

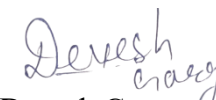**Authors Names:**Vyom Khare, Devesh Garg, Megha Narwan, Surya Pratap Singh, Renuka Bokolia.

Name of conference: Second International Conference on Recent Trends in Applied Physics & Material Science (RAM 2024)

Status of the conference paper: ACCEPTED

Date of communication: 15 April, 2025

Place: Delhi   VyomKhare   Devesh Garg
Date: 09/06/2025   (23/MSCPHY/60)   (23/MSCPHY/18)

This is to certify that the student has incorporated all the corrections suggested by the examiners in the thesis and that the statement made by the candidate is correct to the best of our knowledge.

Dr.RenukaBokolia
(Assistant Professor)

DEPARTMENT OF APPLIED PHYSICS
DELHI TECHNOLOGICAL UNIVERSITY

(Formerly Delhi College of Engineering)

Bawana Road, Delhi-110042

CERTIFICATE

I, hereby certify that the Project Dissertation titled **"Multifunctional Er^{3+}-Doped SrBi$_2$Ta$_2$O$_9$ Ceramics: Optimized Energy Storage and Photoluminescence Properties for Advanced Electronic Applications"** which is submitted by **Vyom Khare**, Roll **No. 23/MSCPHY/60** and **Devesh Garg**, Roll **No. 23/MSCPHY/18,** Department of Applied Physics, Delhi Technological University, Delhi in partial fulfilment of the requirement for the award of the degree of Master of Science, is a record of the project work carried out by the students under my supervision. To the best of my knowledge this work has not been submitted in part or full for any Degree or Diploma to this University or elsewhere.

.

Dr. Renuka Bokolia

Place: Delhi

Date:09/06/2025

<u>Acknowledgement</u>

Abstract

This study systematically investigates the effects of erbium (Er^{3+}) doping on the structural, optical, and electrical properties of $SrBi_2Ta_2O_9$ ceramics to develop next-generation multifunctional materials. Er^{3+}-doped $SrBi_{2-x}Ta_2Er_xO_9$ ceramics (x = 0.00, 0.02, 0.04, 0.06, 0.08) were synthesized using conventional solid-state reaction methods and comprehensively characterized using X-ray diffraction, scanning electron microscopy, Fourier-transform infrared spectroscopy, photoluminescence spectroscopy, and dielectric/ferroelectric measurements. The results demonstrate that Er^{3+} substitution at Bi^{3+} sites preserves the single-phase orthorhombic Aurivillius structure while introducing controlled lattice distortion. Optimal photoluminescence intensity and ferroelectric polarization (P_{max} = 4.57 µC/cm²) were achieved at x = 0.04, exhibiting strong green emission at 524 nm and 549 nm attributed to $^2H_{11/2} \rightarrow {}^4I_{15/2}$ and $^4S_{3/2} \rightarrow {}^4I_{15/2}$ transitions. The x = 0.02 composition demonstrated exceptional energy storage efficiency (η = 95.3–96.8%) across electric fields of 60–80 kV/cm. Dielectric analysis revealed a concentration-dependent transition from normal ferroelectric to relaxor-like behavior, with x = 0.04 approaching complete relaxor characteristics (γ = 1.98427). This work establishes critical structure-property relationships in Er^{3+}-doped SBT ceramics, demonstrating their potential as versatile candidates for high-efficiency energy storage devices and non-volatile ferroelectric memory applications. The demonstrated synergy between structural adaptability and multifunctional performance underscores the transformative potential of rare earth-doped Aurivillius ceramics for next-generation multifunctional materials.

Keywords: Solid-state reaction method, X-ray diffraction, Scanning electron microscopy, Fourier-transform infrared spectroscopy, photoluminescence spectroscopy, Dielectric/Ferroelectricenergy storage devices,Non-volatile ferroelectric memory devices,

Table of Contents

List of tables

List of figures

List of symbols, Abbreviations

SBTO	$SrBi_{2-x}Ta_2Er_xO_9$
XRD	X-ray diffraction
SEM	Scanning electron microscopy
FTIR	Fourier transform infrared spectroscopy
PL	Photo luminescence

CHAPTER 1

Introduction

The development of multifunctional ceramic materials that exhibit both excellent electrical and optical properties has become increasingly important for advanced technological applications in modern electronics, photonics, and energy storage systems. This research focuses on the systematic investigation of Er^{3+}-doped $SrBi_2Ta_2O_9$ ceramics with varying erbium concentrations (x = 0.00, 0.02, 0.04, 0.06, 0.08) to understand how rare earth substitution influences their structural, optical, and electronic properties.

Bismuth Layer-Structured Ferroelectrics: Foundation and Significance

Bismuth layer-structured ferroelectrics (BLSF), also known as Aurivillius phases, represent a fascinating family of materials that have garnered considerable attention since their discovery by Karin Aurivillius in 1949. These materials are characterized by their unique crystal structure, which can be described by the general formula $(Bi_2O_2)^{2+}(A_{m-1}B_mO_{3m+1})^{2-}$, where perovskite blocks $(A_{m-1}B_mO_{3m+1})^{2-}$ are interleaved with bismuth oxide layers $(Bi_2O_2)^{2+}$ along the c-axis. The integer m represents the number of BO_6 octahedra in the perovskite blocks, determining the layer thickness and significantly influencing the material's properties. The bismuth oxide layers serve dual purposes: they provide charge compensation and act as insulating barriers, effectively reducing leakage currents compared to conventional perovskite ferroelectrics.
BLSF materials have emerged as promising lead-free alternatives to traditional lead-based ferroelectrics such as lead zirconate titanate (PZT), addressing growing environmental and health concerns associated with lead-containing materials. These compounds exhibit several advantageous characteristics that make them attractive for technological applications: high Curie temperatures (often exceeding 400°C), excellent fatigue resistance, low coercive fields, and good mechanical quality factors. The layered structure inherently provides structural stability and allows for compositional flexibility, enabling the accommodation of various cations at both A and B sites, which opens pathways for property tuning through strategic substitution.

The significance of BLSF materials extends beyond their ferroelectric properties. Their structural tolerance allows for the incorporation of magnetic ions, making them potential candidates for single-phase multiferroic materials that exhibit simultaneous ferroelectric and magnetic ordering. Additionally, the possibility of incorporating optically active rare earth ions creates opportunities for developing multifunctional materials with combined electrical and optical functionalities, crucial for next-generation optoelectronic devices4.

$SrBi_2Ta_2O_9$: A Promising Two-Layer Aurivillius Compound

Among the BLSF family, $SrBi_2Ta_2O_9$ (SBT) stands out as one of the most extensively studied and technologically relevant compounds. SBT belongs to the two-layer Aurivillius structure (m = 2) and crystallizes in an orthorhombic system with space group $A2_1am$ at room temperature. The crystal structure consists of perovskite blocks containing $SrTa_2O_7$ layers separated by bismuth oxide $(Bi_2O_2)^{2+}$ sheets, with strontium ions occupying twelve-fold coordinated sites between the TaO_6 octahedra.

SBT exhibits exceptional ferroelectric properties that have made it a leading candidate for non-volatile ferroelectric random access memory (FeRAM) applications. The material demonstrates remarkable fatigue endurance, maintaining stable polarization switching over more than 10^{12} cycles, which far exceeds the performance of conventional ferroelectric materials. This outstanding fatigue resistance, combined with low leakage currents and good retention characteristics, positions SBT as an ideal material for practical memory device applications.

The ferroelectric properties of SBT originate from spontaneous polarization arising from canted bismuth-cation displacements, forming both 90° and 180° domain walls. The Curie temperature of SBT is approximately 335°C, indicating excellent thermal stability for high-temperature applications. At room temperature, SBT exhibits a remnant polarization of approximately 5.8 $\mu C/cm^2$ along the a-axis, although this value is lower than that of conventional perovskite ferroelectrics like $BaTiO_3$.

Despite its excellent fatigue resistance and thermal stability, pristine SBT faces certain limitations that restrict its broader application potential. The relatively low spontaneous polarization compared to PZT-based materials and limited optical functionality have motivated researchers to explore compositional modifications to enhance its properties while maintaining its inherent advantages.

Rare Earth Doping Strategy: Er^{3+} as a Multifunctional Dopant

The incorporation of rare earth ions into ferroelectric matrices has emerged as an effective strategy for creating multifunctional materials that combine ferroelectric, optical, and sometimes magnetic properties. Among the rare earth elements, erbium (Er^{3+}) has attracted particular attention due to its unique electronic configuration and optical properties. Er^{3+} ions possess a $4f^{11}$ electronic configuration, which gives rise to sharp emission lines in both the visible and near-infrared regions, making them valuable for photonic applications.

The ionic radius of Er^{3+} (approximately 1.00 Å) is smaller than that of Bi^{3+} (approximately 1.17 Å), allowing for effective substitution at bismuth sites in the Aurivillius structure1. This size difference introduces controlled lattice distortion, which can modify both the ferroelectric and optical properties of the host material. Previous studies have demonstrated that Er^{3+} doping in various ferroelectric systems can enhance polarization values, modify phase transition temperatures, and introduce bright upconversion luminescence.

Er³⁺-doped ferroelectric materials exhibit characteristic green emission bands at approximately 524 nm and 549 nm, corresponding to $^2H_{11/2} \rightarrow {}^4I_{15/2}$ and $^4S_{3/2} \rightarrow {}^4I_{15/2}$ transitions, respectively. These emissions arise from efficient energy transfer processes within the crystal lattice and can be enhanced through optimization of doping concentration and synthesis conditions. The ability to achieve both ferroelectric switching and optical emission in a single material opens new possibilities for integrated optoelectronic devices and multifunctional sensor.

Furthermore, Er³⁺ doping has been shown to influence the microstructural evolution of ferroelectric ceramics. At optimal doping concentrations, typically around 2-4 mol%, Er³⁺ ions can promote grain growth and reduce structural defects, leading to enhanced densification and improved electrical properties1. However, excessive doping can lead to concentration quenching effects, where non-radiative energy transfer between closely spaced Er³⁺ ions reduces the luminescence efficiency.

Research Motivation and Objectives

Despite the promising potential of Er³⁺-doped SBT systems, comprehensive studies investigating the systematic effects of erbium concentration on the structural, optical, and electronic properties remain limited. Understanding the relationship between doping concentration and material properties is crucial for optimizing performance for specific applications. The present research addresses this knowledge gap by conducting a systematic investigation of Er³⁺-doped $SrBi_2Ta_2O_9$ ceramics across a range of erbium concentrations.

The specific objectives of this study include:

1. Investigating the structural evolution and phase stability of SBT upon Er³⁺ substitution,
2. Analyzing the influence of erbium doping on microstructural characteristics and grain morphology,
3. Evaluating the optical properties including photoluminescence behavior and band gap modifications,
4. Characterizing the dielectric and ferroelectric properties as functions of erbium concentration.
5. Establishing structure-property relationships to guide future material design strategies.

This comprehensive characterization approach aims to provide fundamental insights into the Er³⁺ doping effects in Aurivillius-phase materials and contribute to the development of next-generation multifunctional ceramics for advanced technological applications. The results obtained from this systematic study will advance our understanding of rare earth doping strategies in layered ferroelectric materials and pave the way for the rational design of multifunctional ceramic systems with tailored properties.

CHAPTER 2

Synthesis Process for Er³⁺-Doped SrBi₂Ta₂O₉ Ceramics

Er^{3+}-doped $SrBi_{2-x}Ta_2Er_xO_9$ ceramics with varying erbium concentrations (x = 0.00, 0.02, 0.04, 0.06, 0.08) were meticulously synthesized using a conventional solid-state reaction route to ensure phase purity and optimal material properties. High-purity starting materials—strontium carbonate ($SrCO_3$), bismuth oxide (Bi_2O_3), tantalum oxide (Ta_2O_5), and erbium oxide (Er_2O_3)—were accurately weighed in stoichiometric proportions according to the desired composition. These powders were thoroughly mixed and ground together in ethanol for six hours using an agate mortar and pestle. The use of ethanol as a process control agent was crucial, as it not only facilitated uniform mixing at the atomic level but also prevented particle agglomeration, thereby enhancing the homogeneity of the precursor mixture. After drying, the homogenized powder was subjected to calcination at 900°C for three hours in static air. This high-temperature treatment initiated the solid-state reaction necessary to form the layered Aurivillius-phase structure, which was later confirmed by X-ray diffraction (XRD) analysis showing the absence of any secondary phases, thus indicating successful phase formation and effective Er^{3+} incorporation into the lattice.

Following calcination, a 5 wt% polyvinyl alcohol (PVA) binder was added to the powder to improve its mechanical strength and handling during pellet formation. The binder-containing powder was then pressed into disk-shaped pellets under a uniaxial pressure of 50 MPa using a manual hydraulic press, ensuring good compaction and uniform density throughout the samples. The green pellets were subsequently sintered at 1050°C for three hours in an oxygen-rich atmosphere. This sintering process served multiple purposes: it removed any residual organic binder, promoted densification through grain growth and diffusion, and minimized the formation of oxygen vacancies, which is essential for optimizing both the electrical and luminescent properties of the ceramics. The oxygen atmosphere also helped maintain the correct oxidation states of the constituent elements, particularly bismuth, and prevented the reduction of Bi^{3+} ions. The resulting ceramics exhibited a dense microstructure and a single-phase Aurivillius structure, as confirmed by further XRD and microstructural analyses. This detailed synthesis approach ensured the production of high-quality Er^{3+}-doped $SrBi_{2-x}Ta_2Er_xO_9$ ceramics with tailored properties suitable for advanced electronic and optoelectronic applications.
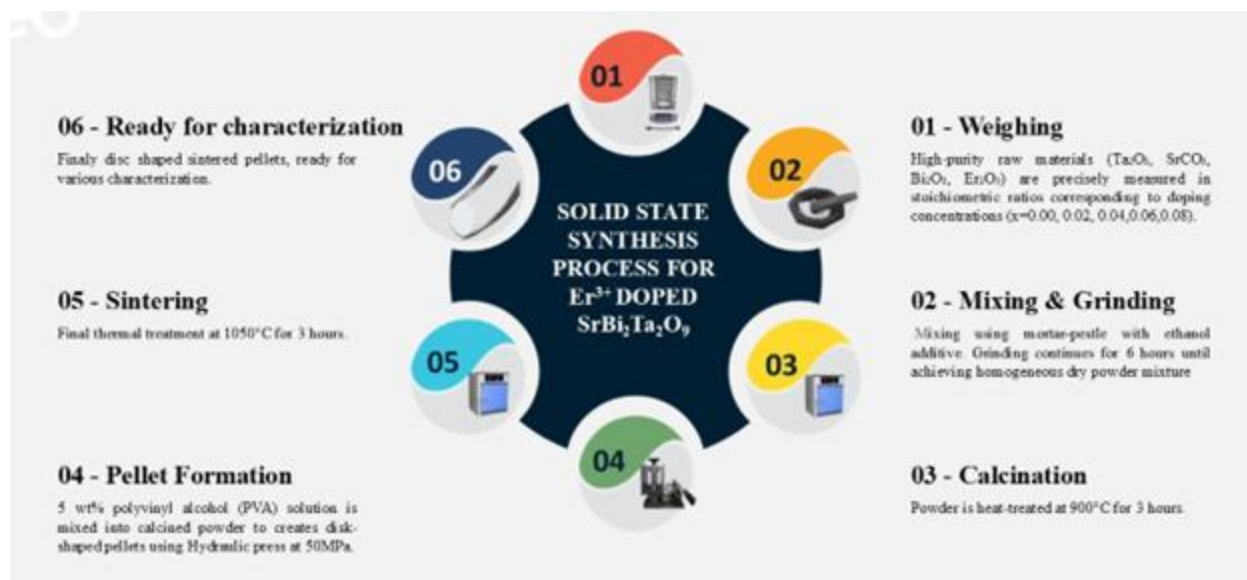
Fig.1. Schematic diagram of the synthesis process.

06 - Ready for characterization
Finaly disc shaped sintered pellets, ready for various characterization.

05 - Sintering
Final thermal treatment at 1050°C for 3 hours.

04 - Pellet Formation
5 wt% polyvinyl alcohol (PVA) solution is mixed into calcined powder to creates disk-shaped pellets using Hydraulic press at 50MPa.

SOLID STATE SYNTHESIS PROCESS FOR Er^{3+} DOPED $SrBi_2Ta_2O_9$

01 - Weighing
High-purity raw materials (Ta_2O_5, $SrCO_3$, Bi_2O_3, Er_2O_3) are precisely measured in stoichiometric ratios corresponding to doping concentrations (x=0.00, 0.02, 0.04,0.06,0.08).

02 - Mixing & Grinding
Mixing using mortar-pestle with ethanol additive. Grinding continues for 6 hours until achieving homogeneous dry powder mixture

03 - Calcination
Powder is heat-treated at 900°C for 3 hours.

CHAPTER 3

Characterization Details of Er^{3+}-Doped $SrBi_2Ta_2O_9$ Ceramics

The comprehensive characterization of Er^{3+}-doped $SrBi_2Ta_2O_9$ ceramics was conducted using multiple analytical techniques to evaluate structural, morphological, optical, and electrical properties. The crystalline structure and phase purity of the synthesized samples were analyzed using X-ray diffraction (XRD) performed on a Bruker D8 Discover X-ray diffractometer. The XRD patterns were recorded over a 2θ range from 10° to 80° to capture all significant Bragg reflections, with measurements conducted at room temperature using Cu Kα radiation to ensure accurate phase identification and lattice parameter determination.

Morphological characterization and surface analysis of the sintered ceramic pellets were performed using scanning electron microscopy (SEM) with a JEOL JSM 6610LV microscope. The SEM imaging provided detailed information about grain size, surface texture, and microstructural features of the ceramic samples. Complementary particle size analysis was conducted using ImageJ software to quantitatively determine average particle dimensions and size distributions from the SEM micrographs, enabling correlation between morphological characteristics and doping concentration effects.

Molecular vibrational analysis was carried out using Fourier-transform infrared (FTIR) spectroscopy with a Perkin Elmer spectrum-II spectrometer1. The FTIR spectra were recorded in the wavenumber range of 400-2600 cm^{-1} to identify characteristic vibrational modes associated with the Aurivillius structure and investigate any systematic changes induced by Er^{3+} incorporation into the host lattice. Optical characterization was performed using two complementary spectroscopic techniques: diffuse reflectance spectroscopy and photoluminescence spectroscopy. UV-Vis-NIR diffuse reflectance spectra were acquired using a JASCO model V-923 spectrophotometer with a spectral resolution of 2 nm, enabling determination of optical band gaps and investigation of Er^{3+} f-f electronic transitions1. Photoluminescence properties were evaluated by recording excitation and emission spectra using an excitation wavelength of λex = 488 nm to assess the luminescent behavior and concentration-dependent quenching effects in the Er^{3+}-doped ceramics.

Electrical characterization encompassed both dielectric and ferroelectric property measurements under controlled conditions. Temperature-dependent dielectric studies were conducted using a Keysight impedance analyzer across a frequency range from 1 kHz to 1 MHz, allowing investigation of frequency dispersion and phase transition behavior. Prior to electrical measurements, ceramic pellets were carefully polished using sandpaper to ensure uniform surface quality, followed by application of air-drying silver paste electrodes to establish reliable electrical contacts while preventing mechanical damage to the delicate samples. Ferroelectric characterization was performed by measuring polarization hysteresis loops using a high-end

automated loop tracer at room temperature under an applied frequency of 20 Hz. These measurements provided quantitative assessment of saturation polarization, remnant polarization, coercive field, and energy storage parameters across different Er^{3+} doping concentrations, enabling evaluation of the materials' potential for energy storage and memory applications.

CHAPTER 4

Characterization Results and Analysis.

In this section we discuss analytical techniques to comprehensively elucidate the structural, morphological, optical, and electrical properties of the synthesized material. X-ray diffraction (XRD) analysis provides critical insights into crystallinity, phase purity, and lattice parameters by probing Bragg diffraction patterns, enabling identification of atomic arrangements and crystallographic defects. Scanning electron microscopy (SEM) complements this by visualizing surface topography, grain boundaries, and microstructural evolution at sub-micron resolution, particularly through secondary electron imaging and backscattered electron detection for compositional contrast. Fourier-transform infrared (FTIR) spectroscopy deciphers molecular bonding configurations and functional groups via characteristic vibrational modes, with attenuated total reflectance (ATR) enhancements improving surface-sensitive measurements. Photoluminescence spectroscopy reveals electronic transitions, defect states, and recombination dynamics through radiative emission profiles, while UV-Vis diffuse reflectance spectroscopy (DRS) quantifies optical bandgap energies and light absorption characteristics through Kubelka-Munk transformations, overcoming scattering limitations in powdered samples. Dielectric and ferroelectric measurements evaluate polarization hysteresis, permittivity, and loss tangents under alternating fields, with careful consideration of interfacial capacitive effects to avoid overestimation of intrinsic material properties. This multimodal approach establishes structure-property correlations by systematically linking atomic-scale ordering (XRD), nanoscale morphology (SEM), molecular interactions (FTIR), optoelectronic behavior (photoluminescence/DRS), and charge transport mechanisms (dielectric), providing a holistic framework for material optimization.

X-ray diffraction (XRD)

X-ray diffraction (XRD) is a cornerstone analytical technique used to investigate the crystallographic structure, phase composition, and physical properties of materials, particularly those that are crystalline in nature. The fundamental principle underlying XRD is the interaction of X-rays with the periodic atomic arrangement in a crystal lattice. When a monochromatic X-ray beam strikes a crystalline sample, the atoms within the lattice scatter the incident X-rays in all directions. Due to the regular spacing of the atomic planes, constructive interference occurs at specific angles, producing a distinct diffraction pattern unique to the material.

The condition for constructive interference is described by Bragg's law:

$$n\lambda = 2d\sin\theta$$

where n is the order of reflection, λ is the wavelength of the incident X-rays, d is the spacing between atomic planes, and θ is the angle of incidence. By measuring the angles and intensities of the diffracted beams, XRD provides detailed information about the interplanar spacings, which can be used to determine lattice parameters, identify crystalline phases, and quantify their relative abundance. This makes XRD highly effective for phase identification, especially in multi-component or polycrystalline materials.

XRD is also employed to estimate crystallite size, assess the degree of crystallinity, and detect structural defects such as dislocations, stacking faults, and strain within the crystal lattice. In addition, advanced techniques like Grazing Incidence XRD (GIXRD) allow for depth profiling in thin films and layered materials, while Rietveld refinement enables precise determination of unit cell dimensions and atomic positions.

The technique is non-destructive, rapid, and versatile, suitable for analyzing powders, thin films, and even small single crystals. It is widely used in materials science, chemistry, geology, electronics, and pharmaceuticals for research, quality control, and failure analysis. The resulting diffraction patterns—typically presented as intensity versus 2θ plots—serve as fingerprints for phase identification and structural analysis.

In summary, XRD is an indispensable tool for elucidating the atomic-scale structure and composition of crystalline materials, providing a foundation for understanding their properties and guiding the development of new material

X-ray diffraction (XRD) Result analysis.

The X-ray diffraction (XRD) analysis of $SrBi_{2-x}Ta_2Er_xO_9$ (x = 0.00–0.08) ceramics provides critical insights into their crystallographic and microstructural evolution upon Er^{3+} doping. All compositions exhibit a **single-phase orthorhombic structure** (space group *A21am*), as confirmed by the close match between observed diffraction patterns and the JCPDS 49-0609 reference. The

absence of secondary peaks across the 2θ range (10°–80°) indicates complete Er^{3+} substitution at Bi^{3+} sites without phase segregation, demonstrating successful solid-solution formation. The dominant **(115)** reflection at 29° aligns with characteristic (112n+1) peaks for n=2 layered Aurivillius phases, consistent with the structural motif of alternating perovskite-like blocks and bismuth oxide layers.

Lattice parameters, calculated using PowderX software, reveal systematic contraction with increasing Er^{3+} content due to the smaller ionic radius of Er^{3+} (1.00 Å) compared to Bi^{3+} (1.17 Å). This substitution-induced strain manifests in **progressive lattice distortion**, quantified by the rising *b/a* ratio from 1.003 (x=0.00) to 1.009 (x=0.08), which directly correlates with octahedral tilting in the perovskite blocks. The measured density reduction (7.85 → 7.62 g/cm³) further supports lattice contraction and suggests potential oxygen vacancy formation to compensate charge imbalance, a common phenomenon in rare-earth-doped Aurivillius systems.

The retained orthorhombic symmetry across all doping levels highlights the structural stability of the host lattice, though the gradual *b/a* increase implies localized symmetry breaking at higher Er^{3+} concentrations. This distortion likely influences ferroelectric polarization by modifying Ti/Ta-O bond angles in the perovskite slabs, while oxygen vacancies may enhance dielectric loss critical considerations for functional property optimization. The results establish a foundation for correlating Er^{3+}-induced structural modifications with optoelectronic and ferroelectric behavior in this material system.

Table 1: Lattice parameters for all the SBT composition ceramic.

Parameters	$SrBi_{2-x}Ta_2Er_xO$				
	SBTOE0	SBTOE2	SBTOE4	SBTOE6	SBTOE8
a (Å)	5.5168	5.5431	5.529	5.5247	5.544
b (Å)	5.5184	5.555	5.5347	5.5649	5.5384
c (Å)	24.7897	24.9339	24.7682	24.9887	24.9176
V (Å³)	754.6954	767.7626	757.9405	768.2627	764.3935
Distortion (b/a)	1.00029	1.002147	1.001031	1.007276	0.99899
Density (g/cm3)	7.92	7.85	7.41	6.95	6.52
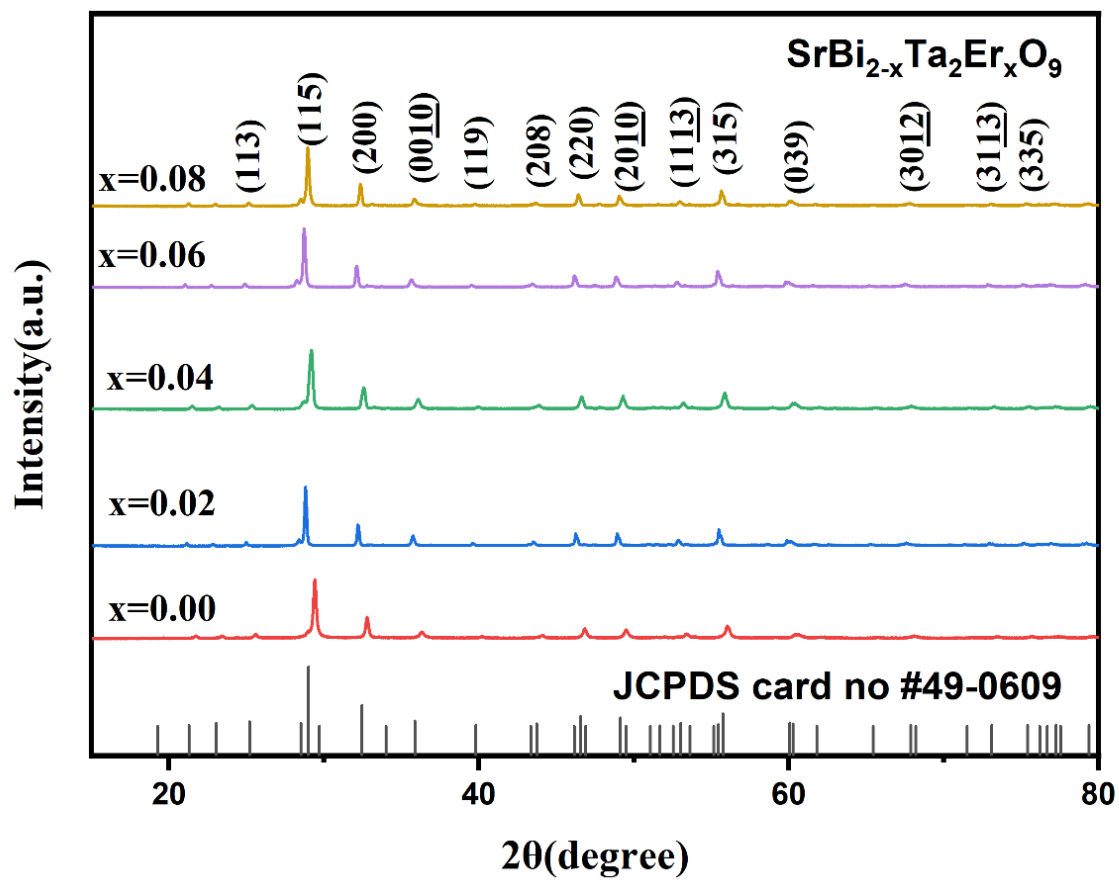
Fig.2. XRD Patterns of Er³⁺-Doped SrBi₂Ta₂O₉ Ceramics with Varying Er Concentrations.

Scanning electron microscopy (SEM)

Scanning electron microscopy (SEM) provides a detailed examination of the surface morphology and microstructural features of Aurivillius-phase ceramics such as $SrBi_{2-x}Ta_2Er_xO_9$. Through high-resolution imaging, SEM reveals the grain size, shape, distribution, and the presence of porosity or intergranular phases, all of which are crucial for understanding the material's sintering behavior and densification. In Aurivillius-type ceramics, the layered structure often manifests as plate-like grains due to the intrinsic anisotropy of the crystal lattice, with grains typically aligning parallel to the (00l) planes. SEM images allow for the direct observation of these features, making it possible to assess the uniformity of grain growth and the effectiveness of the synthesis process. For doped systems, such as those containing Er^{3+}, SEM can highlight changes in grain size and morphology as a function of dopant concentration, often showing that increased dopant levels can inhibit grain growth, leading to finer microstructures. Additionally, SEM combined with energy-dispersive X-ray spectroscopy (EDS) can be used to verify the elemental composition and the homogeneous distribution of dopants within the grains. The microstructural integrity observed in SEM images is closely linked to the material's functional properties, such as dielectric and ferroelectric performance, since grain boundaries and defects can act as scattering centers for charge carriers or as pinning sites for domain walls. Thus, SEM analysis not only provides visual confirmation of phase purity and structural uniformity but also offers insights into the relationships between processing, microstructure, and the resulting physical properties of the material.

SEM: Results and analysis:

The scanning electron microscopy (SEM) analysis of $SrBi_{2-x}Ta_2Er_xO_9$ (x = 0.00–0.08) sintered pellets provides critical insights into the relationship between Er^{3+} doping concentration, microstructural evolution, and luminescent properties. The SEM micrographs reveal a **randomly oriented plate-like morphology**, characteristic of bismuth-layered Aurivillius-phase ferroelectrics (BLSF), with distinct grain growth patterns influenced by Er^{3+} substitution. For the undoped composition (x = 0.00), the average particle size, quantified via ImageJ software, measures **1.986 μm**, while at x = 0.04, this increases to **2.192 μm**, correlating with the **maximum observed photoluminescence intensity**. This size enhancement arises from Er^{3+} ions optimally occupying Bi^{3+} lattice sites at 4% doping, reducing structural defects such as vacancies, dislocations, and grain boundaries that typically impede coherent crystal growth. The substitution of smaller Er^{3+} ions (1.00 Å) for Bi^{3+} (1.17 Å) introduces controlled lattice strain, which promotes grain coalescence by lowering interfacial energy barriers. Larger particles exhibit smoother surfaces and fewer defects, minimizing non-radiative recombination pathways that dissipate energy as heat rather than light.

However, exceeding the 4% Er^{3+} threshold (x > 0.04) reverses this trend, with particle size decreasing to 1.287 μm at x = 0.08. This reduction stems from **lattice strain saturation** and **site-blocking effects**—excessive Er^{3+} ions create localized stress fields that hinder atomic diffusion

during sintering, while dopant clustering at grain boundaries fragments growing crystallites. Concurrently, **concentration quenching** emerges due to reduced interionic distances between Er^{3+} activators. At high doping levels, excited-state energy migrates between neighboring Er^{3+} ions via non-radiative dipole-dipole interactions, dissipating energy through phonon emissions rather than radiative transitions. This is exacerbated by defect proliferation from charge compensation mechanisms (e.g., oxygen vacancy formation to balance Er^{3+} substitution), which introduce mid-gap states that trap charge carriers.

The microstructural evolution directly correlates with luminescent performance. The 4% Er^{3+} sample's larger grains provide fewer scattering centers for photons and excitons, enhancing light output. In contrast, the $x = 0.08$ composition's smaller grains and higher defect density create a heterogeneous energy landscape, fragmenting emission pathways. These findings align with studies on rare-earth-doped Aurivillius phases, where optimal doping balances lattice compatibility and activator separation to maximize radiative efficiency. The SEM-derived particle size distribution, presented as histograms in Fig.2., further validates the narrow size dispersion at $x = 0.04$, indicating uniform dopant integration—a prerequisite for applications in optoelectronic devices requiring consistent emission characteristics.
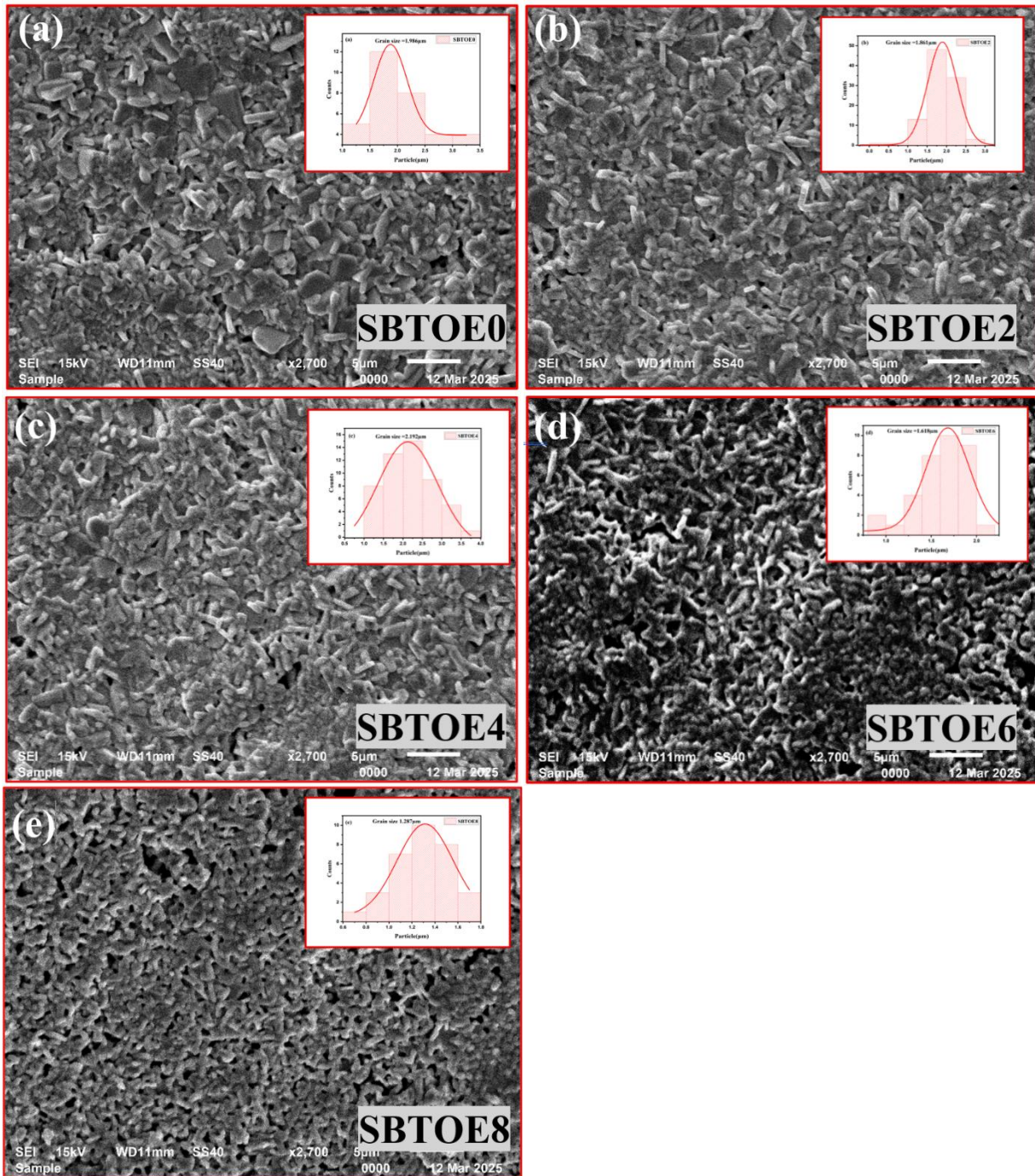
Fig.3.SEM images and particle size distributions of SrBi$_2$Ta$_2$O$_9$:Er^{3+} ceramics: (a) undoped (0.00), (b) 0.02, (c) 0.04, (d) 0.06, and (e) 0.08 Er^{3+} concentrations.

Fourier-transform infrared spectroscopy (FTIR)

Fourier-transform infrared spectroscopy (FTIR) is a powerful analytical technique used to probe the molecular structure, chemical bonding, and functional groups present in a material by measuring its absorption or transmission of infrared (IR) radiation across a broad spectral range, typically spanning 4000–400 cm^{-1}. The fundamental principle of FTIR revolves around the interaction of IR light with molecular vibrations, which occur when the frequency of the incident IR radiation matches the natural vibrational frequency of specific chemical bonds within the sample. These vibrations include stretching (symmetric and asymmetric) and bending (scissoring, rocking, wagging, twisting) modes, each corresponding to characteristic energy transitions that produce absorption bands in the IR spectrum. The technique operates on the basis of the Michelson interferometer, which replaces the traditional dispersive elements (e.g., prisms or gratings) used in conventional infrared spectroscopy. In an FTIR instrument, a broadband IR source emits light that is split into two beams by a beam splitter: one beam reflects off a fixed mirror, while the other travels to a moving mirror. The recombined beams create an interferogram—a time-dependent signal resulting from the constructive and destructive interference of the two beams—which is then Fourier-transformed by the instrument's software to generate a spectrum of intensity versus wavenumber (cm^{-1}). This interferometric approach offers significant advantages over dispersive methods, including higher signal-to-noise ratios (due to the Fellgett advantage, which allows simultaneous measurement of all frequencies), faster data acquisition (enabling real-time monitoring of dynamic processes), and improved wavelength accuracy (via He-Ne laser calibration of the mirror movement).

Quantitative analysis in FTIR is facilitated by the Beer-Lambert law, which relates absorbance (A) to concentration (c), path length (l), and molar absorptivity (ε):

$$A = \varepsilon c l$$

By constructing calibration curves using standard samples, FTIR can determine dopant concentrations or quantify phase fractions in multiphase systems. However, challenges such as overlapping peaks (e.g., Bi–O and Ta–O vibrations in Aurivillius phases) often necessitate advanced spectral deconvolution techniques, such as Gaussian/Lorentzian curve fitting or multivariate analysis (e.g., partial least squares regression), to extract accurate compositional data.

Fourier Transform Infrared (FTIR): results and analysis:

The Fourier Transform Infrared (FTIR) spectroscopy analysis of Er^{3+}-doped $SrBi_{2-x}Ta_2Er_xO_9$ ceramics provides valuable insights into the evolution of the local bonding environment and structural integrity of the Aurivillius phase upon rare-earth doping. The FTIR spectra, recorded in the range of 400–2600 cm^{-1}, exhibit prominent absorption features that are characteristic of the layered perovskite structure. The most intense and defining band appears around 600–650 cm^{-1} in

all samples, which is attributed to the stretching vibrations of Ta–O bonds within the TaO_6 octahedra—a signature vibrational mode for $SrBi_2Ta_2O_9$. This band's presence and intensity confirm the preservation of the fundamental Aurivillius framework across all doping concentrations. In the medium-frequency region, another notable band is observed near 560 cm^{-1}, which arises from a combination of Sr–O stretching and lower-frequency Ta–O bending modes, further supporting the structural stability of the perovskite blocks. As the Er^{3+} content increases from x = 0.00 to x = 0.08, subtle yet systematic changes become evident in the FTIR spectra. Specifically, the dominant Ta–O stretching band exhibits progressive broadening and slight shifts in peak position, indicative of controlled lattice distortion and increased disorder within the TaO_6 octahedra. These spectral modifications are a direct consequence of the successful incorporation of the smaller Er^{3+} ions into the Bi^{3+} sites, which introduces local strain and alters the vibrational dynamics of the surrounding lattice. Importantly, the absence of new absorption bands or significant changes in the spectral profile suggests that Er^{3+} doping does not disrupt the overall Aurivillius structure or lead to the formation of secondary phases. Instead, the observed changes reflect a fine-tuning of the local structure, with Er^{3+} ions subtly modifying the octahedral environment while maintaining the integrity of the layered perovskite architecture. This detailed spectroscopic analysis not only confirms the effective substitution of Er^{3+} into the $SrBi_2Ta_2O_9$ lattice but also highlights the sensitivity of FTIR to detect even minor structural distortions, which are crucial for understanding and optimizing the material's functional properties.
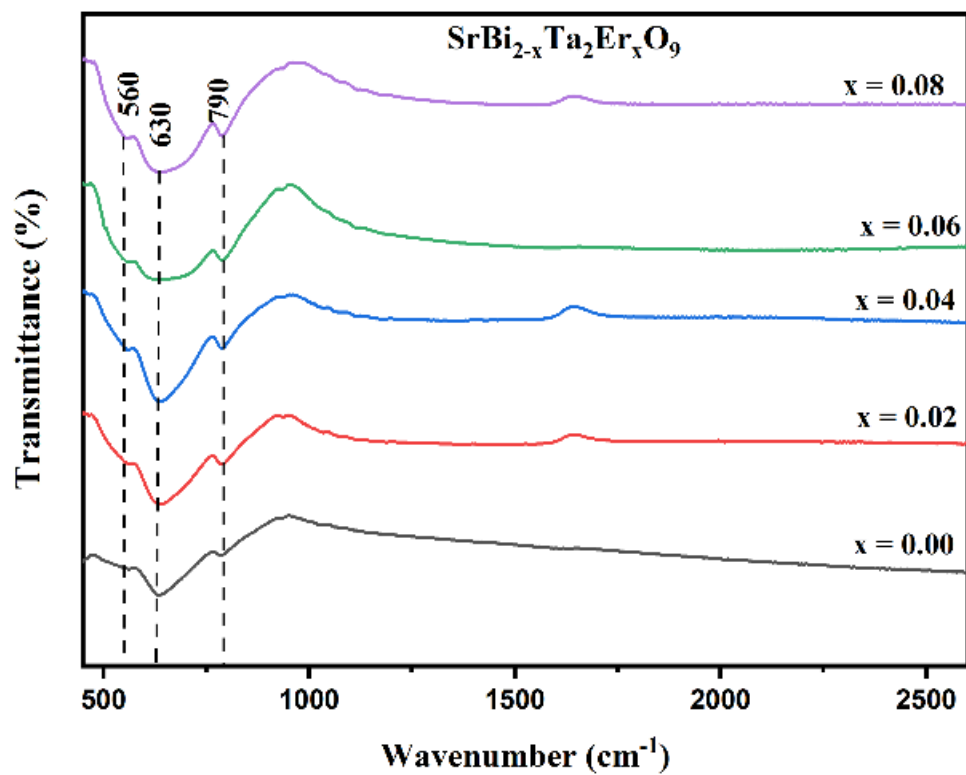
Fig.4. FTIR Spectra of Er^{3+}-Doped SrBi$_2$Ta$_2$O$_9$ Ceramics (x = 0.00–0.08).
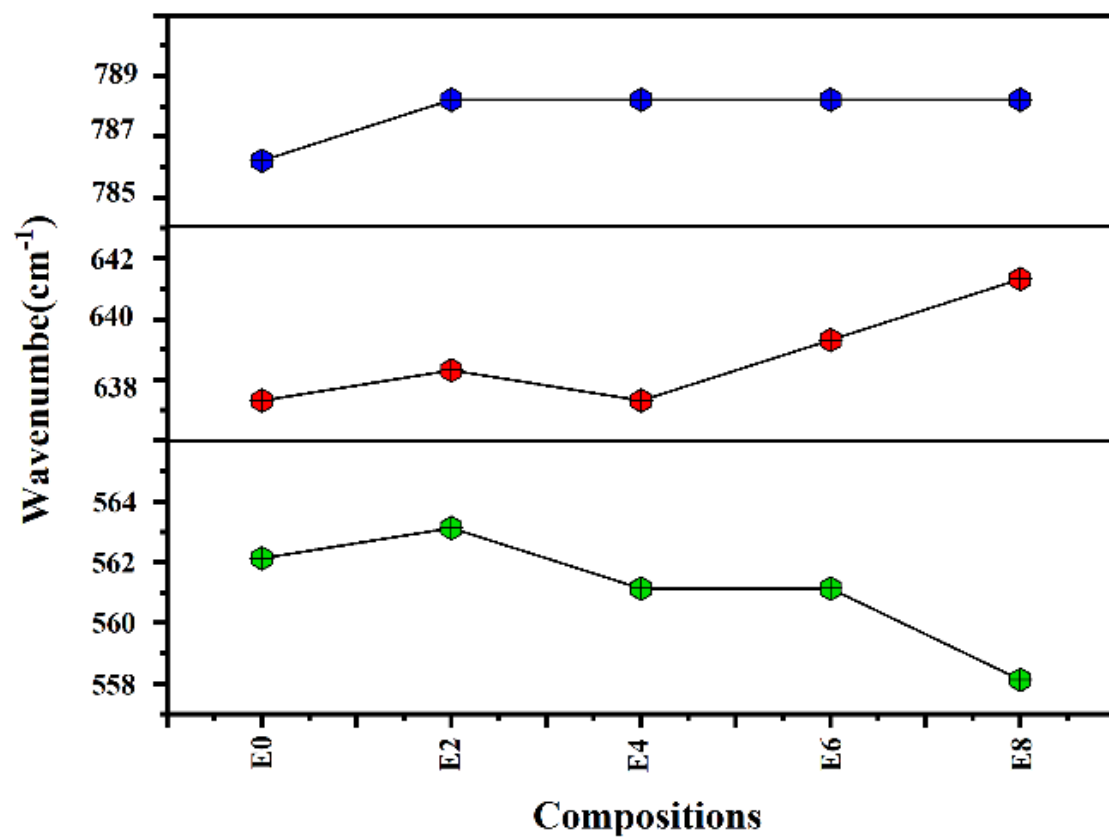
Fig.5. Concentration-Dependent FTIR Absorption Bands in $SrBi_2Ta_2O_9$:Er^{3+} Ceramics.

Photoluminescence (PL) spectroscopy

Photoluminescence (PL) spectroscopy is a highly sensitive, non-destructive technique used to probe the electronic and optical properties of materials, particularly semiconductors, insulators, and luminescent ceramics. The fundamental principle of PL involves the excitation of a material by photons—typically from a laser or lamp whose energy exceeds the material's bandgap or electronic transition energies. When these photons are absorbed, electrons in the material are promoted from lower energy states (such as the valence band in semiconductors) to higher energy states (such as the conduction band), leaving behind positively charged "holes." This excited state is unstable, and the system relaxes as electrons lose energy through various pathways. Some of this relaxation occurs non-radiatively, where energy is dissipated as heat or through lattice vibrations (phonons), but a significant portion can occur radiatively: electrons recombine with holes, releasing energy in the form of emitted photons. This emission of light as the material returns to its ground state is called photoluminescence.

The PL spectrum intensity of emitted light as a function of wavelength or energy—provides rich information about the material. The position of the PL emission peak directly relates to the bandgap energy in semiconductors or to specific electronic transitions in doped materials. The shape and width of the PL peak can reveal the presence of defects, impurities, or inhomogeneities, as well as the quality and crystallinity of the sample. For example, a narrow, intense PL peak is typically a sign of high material quality with few non-radiative recombination centers, while broad or multiple peaks may indicate the presence of defect states or compositional fluctuations. In materials doped with rare-earth ions, such as Er^{3+}-doped $SrBi_2Ta_2O_9$, PL can be used to study the efficiency of energy transfer to the dopant ions and the resulting emission from their characteristic energy levels.

PL spectroscopy can also distinguish between different types of radiative processes: fluorescence and phosphorescence. Fluorescence occurs when the emission happens almost instantaneously (within nanoseconds) after excitation, while phosphorescence involves longer-lived excited states and delayed emission. The quantum yield of PL, defined as the ratio of emitted to absorbed photons, is a key parameter for evaluating the efficiency of luminescent materials and optoelectronic devices.

A notable feature of PL is the Stokes shift, which refers to the difference in energy (or wavelength) between the absorbed and emitted photons. After excitation, electrons typically relax to the lowest vibrational level of the excited state before emission, so the emitted photon has less energy than the absorbed one. This shift provides insight into vibrational relaxation processes and the interaction of electronic states with the lattice.

PL spectroscopy is widely used in research and industry for characterizing band structure, identifying impurity and defect states, evaluating the quality of thin films and nanomaterials, and optimizing the performance of devices such as LEDs, lasers, and solar cells. Advanced PL

techniques, such as time-resolved PL (TRPL), can measure the lifetimes of excited states, providing further information about recombination dynamics and non-radiative processes. By combining PL with other techniques like Raman spectroscopy, researchers can obtain complementary information about both the electronic and vibrational properties of materials on a single platform.

In summary, photoluminescence spectroscopy is an indispensable tool for the detailed analysis of the optical and electronic behavior of materials. Its ability to sensitively detect changes in band structure, defect levels, and energy transfer processes makes it essential for the development and optimization of advanced functional materials and optoelectronic devices.

Photoluminescence (PL) spectroscopy: results and analysis.

The photoluminescence (PL) properties of Er^{3+}-doped $SrBi_{2-x}Ta_2Er_xO_9$ ceramics, as depicted in Fig.6. (a, b), highlight the material's strong and tunable green emission, making it highly promising for photonic device applications. The excitation spectrum, monitored at the emission maximum of 550 nm, shows a pronounced peak at 488 nm, indicating that this wavelength is most effective for exciting Er^{3+} ions within the host lattice. When the ceramics are excited at 488 nm, the emission spectrum reveals two prominent green emission peaks at 524 nm and 549 nm, which correspond to the $^2H_{11/2} \rightarrow {}^4I_{15/2}$ and $^4S_{3/2} \rightarrow {}^4I_{15/2}$ transitions of Er^{3+}, respectively. The 549 nm emission is notably the most intense, arising from the efficient population and subsequent radiative relaxation of the $^4S_{3/2}$ energy level, which is a hallmark of effective energy transfer and minimal non-radiative losses in the system. Between 524 nm and 549 nm, the emission features are further split into multiple components due to the Stark effect, which is a direct result of the crystal field interactions and symmetry distortions experienced by Er^{3+} ions in the layered Aurivillius lattice. In addition to the dominant green emission, a weak red emission band is observed at 660 nm, attributed to secondary energy transfer processes, such as transitions from the $^4F_{9/2}$ to $^4I_{15/2}$ state. As the Er^{3+} doping concentration increases, the PL intensity initially rises, reaching a maximum at x = 0.04, which suggests that this is the optimal concentration for maximizing luminescence. This increase can be attributed to more Er^{3+} ions being available for excitation and emission without significant non-radiative losses. However, beyond this concentration, the PL intensity decreases due to concentration quenching, where the proximity of Er^{3+} ions facilitates non-radiative energy transfer between them, thus reducing the overall emission efficiency. Importantly, the emission wavelengths remain unchanged across all doping levels, indicating that the local environment of Er^{3+} ions within the host lattice is preserved and that the quenching mechanism is primarily due to energy migration rather than structural changes or phase segregation. These findings demonstrate that Er^{3+}-doped $SrBi_{2-x}Ta_2Er_xO_9$ ceramics exhibit robust and stable green emission, with optimal performance at moderate doping levels, making them excellent candidates for use as green light phosphors in advanced photonic and optoelectronic devices.
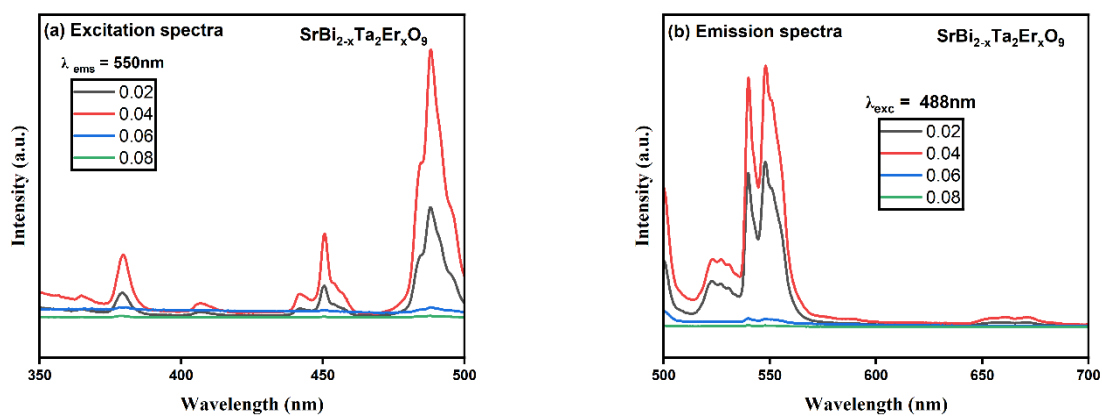
Fig.6. Photoluminescence Excitation and Emission Spectra of SrBi$_2$Ta$_2$O$_9$:Er^{3+} Ceramics as a Function of Er^{3+} Concentration: (a) Excitation spectra monitored at 550nm emission (b) Emission spectra under 488nm excitation

Diffuse reflectance spectroscopy (DRS)

Diffuse reflectance spectroscopy (DRS) is a critical technique for determining the optical band gap (Eg) of materials, particularly powders, ceramics, and nanostructures. It is is a widely used technique for investigating the optical properties and determining the band gap of powdered, polycrystalline, or nanostructured materials, especially when traditional transmission measurements are not feasible. In DRS, the intensity of light diffusely reflected from a sample is measured and compared to a non-absorbing reference, often $BaSO_4$, to obtain the reflectance spectrum. This reflectance data is then transformed using the Kubelka-Munk function, which relates the reflectance to the absorption and scattering coefficients of the material and serves as an analogue to the absorption coefficient in transmission measurements.

To calculate the optical band gap using Diffuse Reflectance Spectroscopy (DRS) data, the Kubelka-Munk function and Tauc plot method are were employed. The reflectance spectrum (R) is transformed into the absorption coefficient using the Kubelka-Munk equation[s 50].

$$F(R) = \frac{(1 - R^2)}{2R} = \frac{\alpha}{S}$$

Where α is the absorption coefficient, R represents the reflectance of samples and S stands for scattering coefficient. This transformation is critical because direct reflectance data alone cannot isolate the material's absorption properties. Next, the Tauc plot method is applied to relate the absorption coefficient to photon energy (hv). The general form of the Tauc equation is [s 50]

$$F(R)hv = C(hv - E_g)^n$$

Here, E_g is the band gap energy, n is an exponent determined by the electronic transition type (e.g., n=2 for indirect allowed transitions, n=1/2 for direct allowed transitions) [s 51], and C is a proportionality constant. To generate the Tauc plot, photon energy (hv) is calculated from the wavelength (λ) using:

$$hv = \frac{1239.7}{\lambda \, (nm)} \, (in \; eV)$$

Diffuse reflectance spectroscopy (DRS): Result and analysis:

The optical properties of $SrBi_{2-x}Ta_2Er_xO_9$ ceramics with varying Er^{3+} concentrations (x = 0.00, 0.02, 0.04, 0.06, and 0.08) were thoroughly examined using UV-Visible diffuse reflectance spectroscopy (DRS), revealing how Er^{3+} doping modulates both the absorption features and the material's band gap. The DRS spectra display a series of well-defined troughs, or absorption bands, whose intensity increases with higher Er^{3+} content. These troughs are attributed to the characteristic f-f electronic transitions of Er^{3+} ions, specifically from the ground state $^4I_{15/2}$ to various excited states, as detailed by Carnall et al. (1968). The presence and intensification of these absorption

features confirm the successful incorporation of Er³⁺ into the Aurivillius lattice and reflect the growing influence of Er³⁺ crystal field interactions within the host structure.

Table 2: Wavelength of Absorption Bands and there Corresponding Electronic Transition of Er^{+3} in $SrBi_{2-x}TaEr_xO_9$.

Region	Wavelength of absorption bands	Electronic transitions
Ultraviolet Region (200-400 nm)	350 nm	$^4I_{15/2} \rightarrow {}^4G_{9/2}$
Green-Yellow Region (490-570 nm)	520 nm	$^4I_{15/2} \rightarrow {}^4F_{5/2}$
Red Region (600-700 nm)	650 nm	$^4I_{15/2} \rightarrow {}^4F_{9/2}$
Near Infrared Region (700-800 nm)	800 nm	$^4I_{15/2} \rightarrow {}^4I_{9/2}$

To determine the optical band gap, the reflectance data were transformed using the Kubelka-Munk function and analyzed through Tauc plots in fig.7., where $[F(R)h\nu]^{1/2}$ was plotted against photon energy ($h\nu$). The linear region of each plot was extrapolated to intersect the energy axis, yielding the band gap energies for each composition. The results show that the band gap values for $SrBi_{2-x}Ta_2Er_xO_9$ are 2.74, 2.73, 2.86, 2.66, and 3.46 eV for x = 0.00, 0.02, 0.04, 0.06, and 0.08, respectively. Interestingly, the band gap initially increases with moderate Er³⁺ doping (peaking at x = 0.04), possibly due to improved crystallinity and reduced defect density, before decreasing at x = 0.06, likely as a result of defect-related mid-gap states introduced by higher dopant concentrations. At the highest doping level (x = 0.08), the band gap sharply increases, which may be attributed to significant structural changes or quantum confinement effects as the lattice accommodates more Er³⁺ ions. Overall, these findings demonstrate that Er³⁺ doping not only introduces characteristic absorption bands but also enables precise tuning of the optical band gap in $SrBi_2Ta_2O_9$:Er³⁺ ceramics, making them promising materials for optoelectronic and photonic applications where band gap engineering is essential.
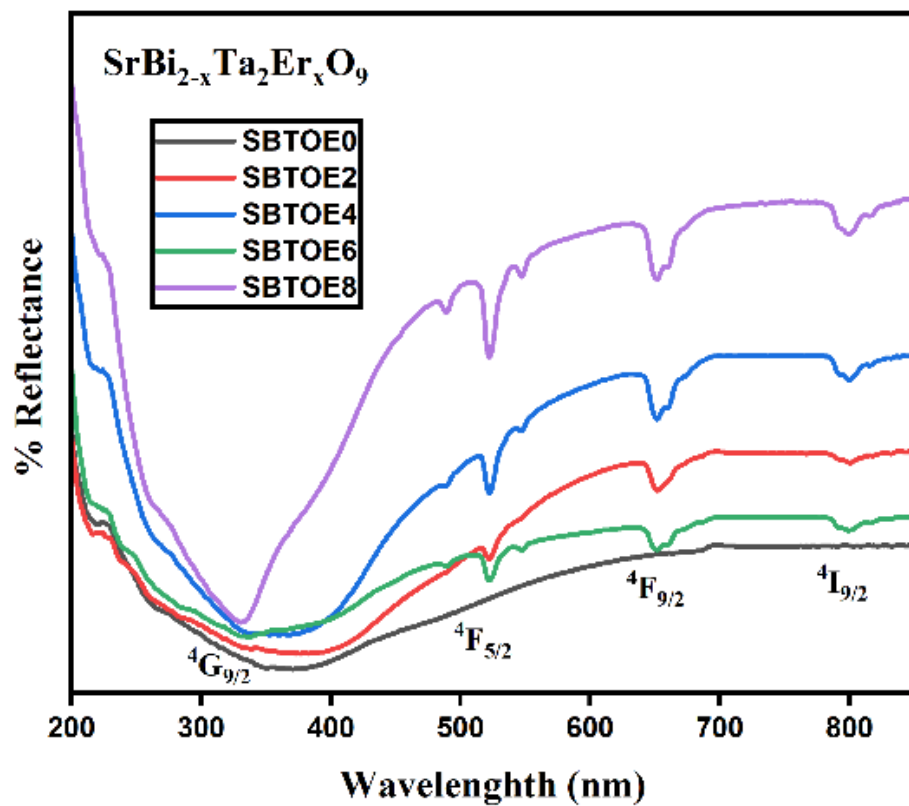
Fig.7. Diffuse Reflectance Spectra of in SrBi₂Ta₂O₉:Er³⁺ Ceramics: Correlating Dopant Concentration with Absorption curve broadening.
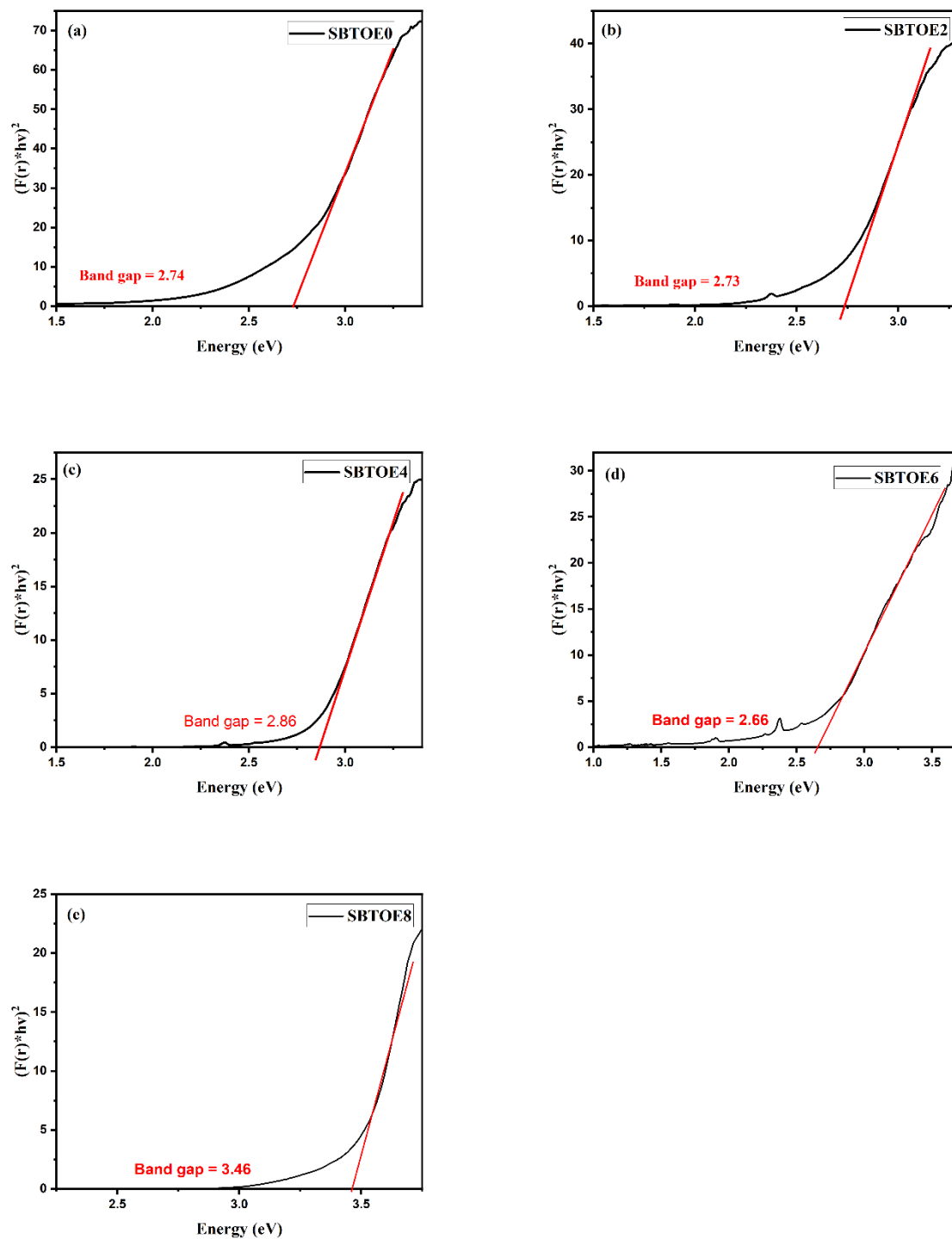
Fig.8. Tauc plot and Band Gap analysis of $SrBi_2Ta_2O_9{:}Er^{3+}$ ceramics: (a) undoped (0.00), (b) 0.02, (c) 0.04, (d) 0.06, and (e) 0.08 Er^{3+} concentrations.

Dielectric characterization:

The dielectric characterization of Aurivillius-phase ceramics, such as Er^{3+}-doped $SrBi_{2-x}Ta_2Er_xO_9$, provides critical insights into their polarization dynamics, charge transport mechanisms, and potential for energy storage or multiferroic applications. These properties are intricately linked to the material's layered structure, defect chemistry, and dopant-induced modifications.

The dielectric properties of Aurivillius-phase ceramics, such as permittivity (ε'), dielectric loss ($\tan\delta$), and diffuseness parameter (γ), are critical for understanding their polarization dynamics and phase transitions. **Permittivity (ε')** reflects the material's ability to store electrical energy and typically decreases with increasing frequency due to suppressed dipolar reorientation at higher frequencies. In Er^{3+}- doped systems, ε' reduction is linked to dopant-induced structural modifications, such as decreased oxygen vacancy density and lattice strain.

The **diffuseness parameter (γ)**, derived from the modified Curie-Weiss law, quantifies the breadth of phase transitions. For ideal ferroelectrics, $\gamma = 1$, while relaxor behavior corresponds to $\gamma \approx 2$. The parameter γ thus serves as a bridge between structural heterogeneity and relaxor-like dielectric responses, enabling tailored design of materials for energy storage or sensor applications

Dielectric: Result and analysis.

The Fig.9. (a-e), Fig.10 (a-e), Fig.11. (a-e) encompasses detailed characterization of dielectric constant, dielectric loss, and diffuseness parameter (γ) across multiple frequencies and temperatures, providing crucial insights into the ferroelectric-to-paraelectric phase transition behavior and the influence of rare earth substitution on the fundamental dielectric properties of $SrBi_{2-x}Ta_2Er_xO_9$ (x = 0.00, 0.02, 0.04, 0.06, and 0.08). Dielectric Constant (ε') decreases with increasing frequency (5 kHz $\rightarrow$ 1000 kHz) for all doping levels, a hallmark of relaxor ferroelectric behavior where dipoles struggle to align with rapidly alternating fields. For undoped $SrBi_2Ta_2O_9$, the dielectric constant reaches maximum values ~950 approaching at the Curie temperature, particularly at low frequencies. The sharp transition observed at the Curie temperature indicates a relatively abrupt phase change from the ferroelectric orthorhombic state to the paraelectric tetragonal phase, consistent with prior literature reports for bismuth-layered Aurivillius compounds.The reduction in dielectric constant and progressive peak broadening observed in $SrBi_2Ta_2O_9$ with increasing Er^{3+} doping concentration are attributed to Er^{3+} incorporation at Bi^{3+} site. This substitution generates oxygen vacancies and lattice strain, thereby impeding domain wall motion and promoting localized polar regions.

The dielectric loss (ε'') characteristics, as shown in Fig.10 (a-e), indicate that as the temperature approaches and exceeds the Curie temperature (approximately 370°C for $SrBi_2Ta_2O_9$), the dielectric loss behavior becomes dominated by the ferroelectric phase transition. In the undoped material, a sharp increase in dielectric loss is observed near the Curie temperature, primarily due to enhanced domain wall motion and increased ionic conductivity. However, with the introduction of Er^{3+} doping, the Er^{3+} ions incorporate at Bi^{3+} sites, leading to the generation of oxygen vacancies

and lattice strain. This results in the pinning of domain walls, which reduces their mobility and consequently decreases the dielectric loss associated with domain wall motion. As evident from Fig.12., the dielectric loss decreases progressively with increasing Er^{3+} concentration. For the frequency range (5khz – 1000khz) dipolar relaxation becomes the primary loss mechanism, Fig.10 (a-e) shows a systematic reduction in dielectric loss with increasing frequency across all doping concentrations. This trend can be attributed to the inability of polarization mechanisms such as space charge accumulation, orientational polarization, and ionic displacement to effectively respond to the rapidly alternating electric field at higher frequencies, resulting in decrease in dielectric loss.

The diffuseness parameter (γ) is a crucial measure that quantifies how "spread out" or diffuse a phase transition is in ferroelectric materials. It tells us whether a material undergoes a sharp, well-defined phase transition or a gradual, broadened one. The diffuseness parameter is calculated using the modified Curie-Weiss law.

$$\frac{1}{\varepsilon'} - \frac{1}{\varepsilon'_m} = C^{-1}(T - T_m)^{\gamma}$$

Where, ε' represents the dielectric constant at a given temperature T, while ε'_m denotes the maximum dielectric constant observed at the transition temperature T_m. The parameter C refers to the Curie-Weiss constant, which characterizes the material's polarizability and γ is the diffuseness parameter. The parameter γ is determined from the slope of the plot, $\left[\frac{1}{\varepsilon'} - \frac{1}{\varepsilon'_m}\right]$ vs $ln(T - T_m)$. Where γ ≈ 1 indicates an ideal sharp ferroelectric transition and γ ≈ 2 represents complete relaxor behavior .

The calculated γ values Fig.11. (a-e), show interesting non-monotonic behavior with Er^{3+} concentration, The maximum γ value of 1.93102 observed at x = 0.04 suggests this composition represents a critical concentration where the system exhibits the strongest relaxor characteristics. This value approaches the theoretical limit of γ = 2 for complete relaxor behavior, indicating substantial disorder in the ferroelectric transition at this particular compositionInterestingly, the γ values for x = 0.06 and 0.08 decrease slightly to around 1.75, suggesting a stabilization of the diffuse transition character rather than continued enhancement. This behavior may indicate that beyond a certain threshold concentration, the Er^{3+} substitution reaches a saturation limit in terms of its ability to induce disorder, possibly due to clustering effects or preferential site occupation.

To conclude at x= 0.04 critical threshold is observed, where ε_{max} drops to ~600, and the transition becomes markedly diffuse, evidenced by a diffuseness parameter (γ) of 1.93102 approaching the relaxor limit (γ = 2). This indicates a crossover from normal ferroelectric to relaxor-like behavior, driven by Er^{3+}-mediated local structural in homogeneity and weakened dipolar ordering. These findings underscore the role of Er^{3+} in tailoring the dielectric response, with x = 0.04 representing an optimal balance between compositional disorder and retained ferroelectricity.
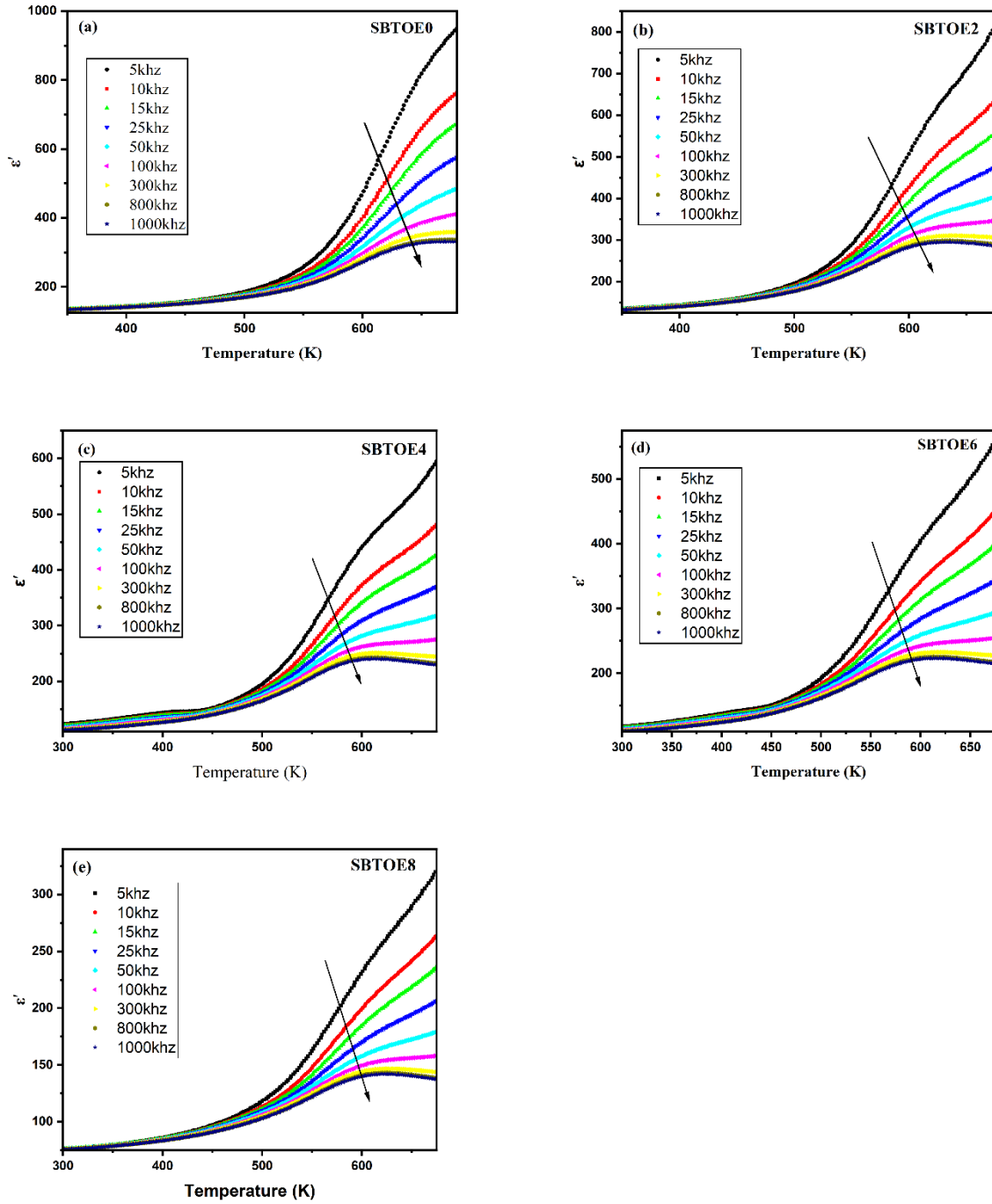
Fig.9. Dielectric constant (ε') vs. temperature profiles SrBi$_2$Ta$_2$O$_9$:Er^{3+} at various frequencies from 5 kHz–1 MHz: (a) undoped (0.00), (b) 0.02, (c) 0.04, (d) 0.06, and (e) 0.08 Er^{3+} concentrations.
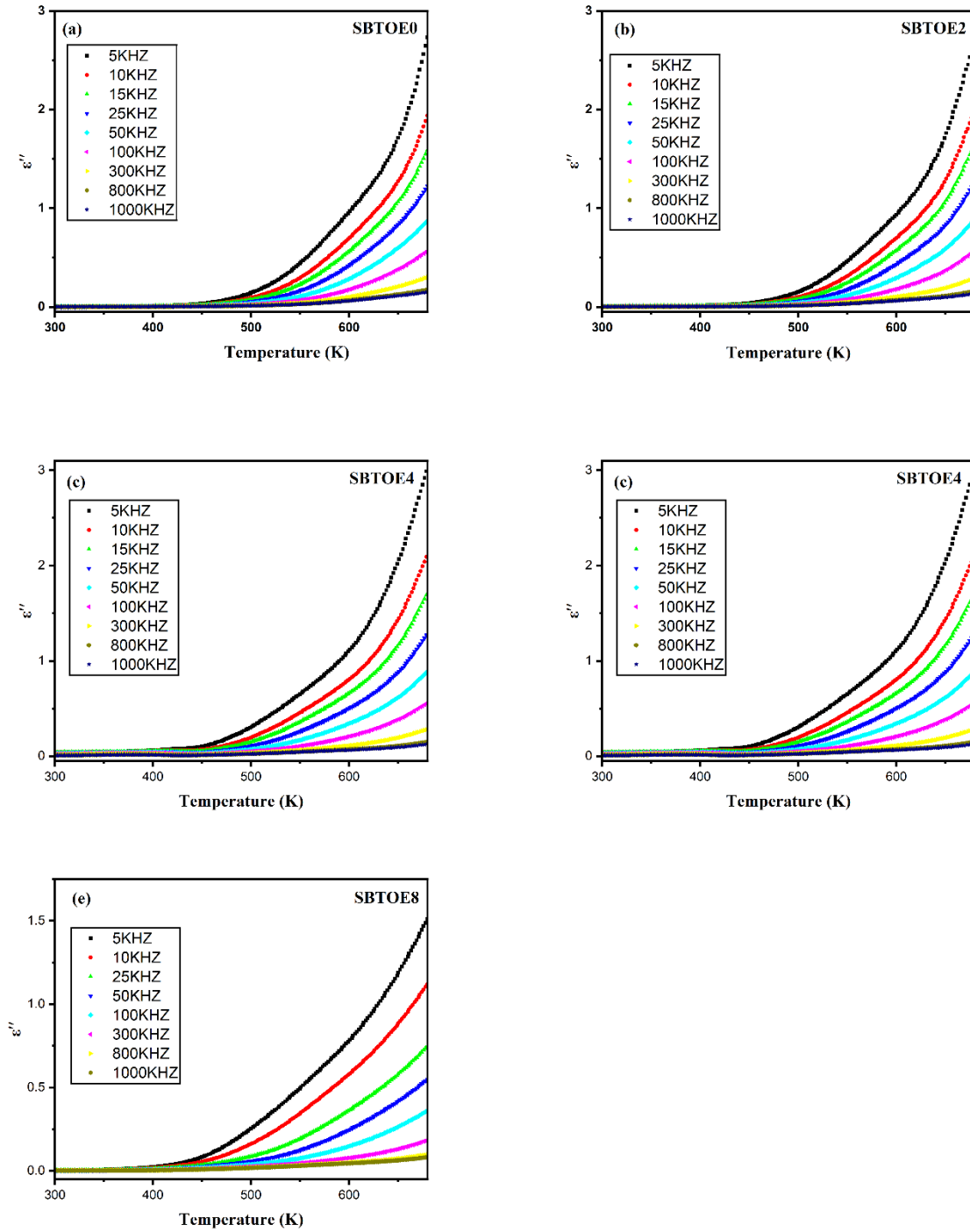
Fig.10. Temperature-dependent dielectric loss in $SrBi_2Ta_2O_9:Er^{3+}$ for various frequencies 5khz-1Mhz: (a) 0.00, (b) 0.02, (c) 0.04, (d) 0.06, (e) 0.08 Er^{3+} concentrations.
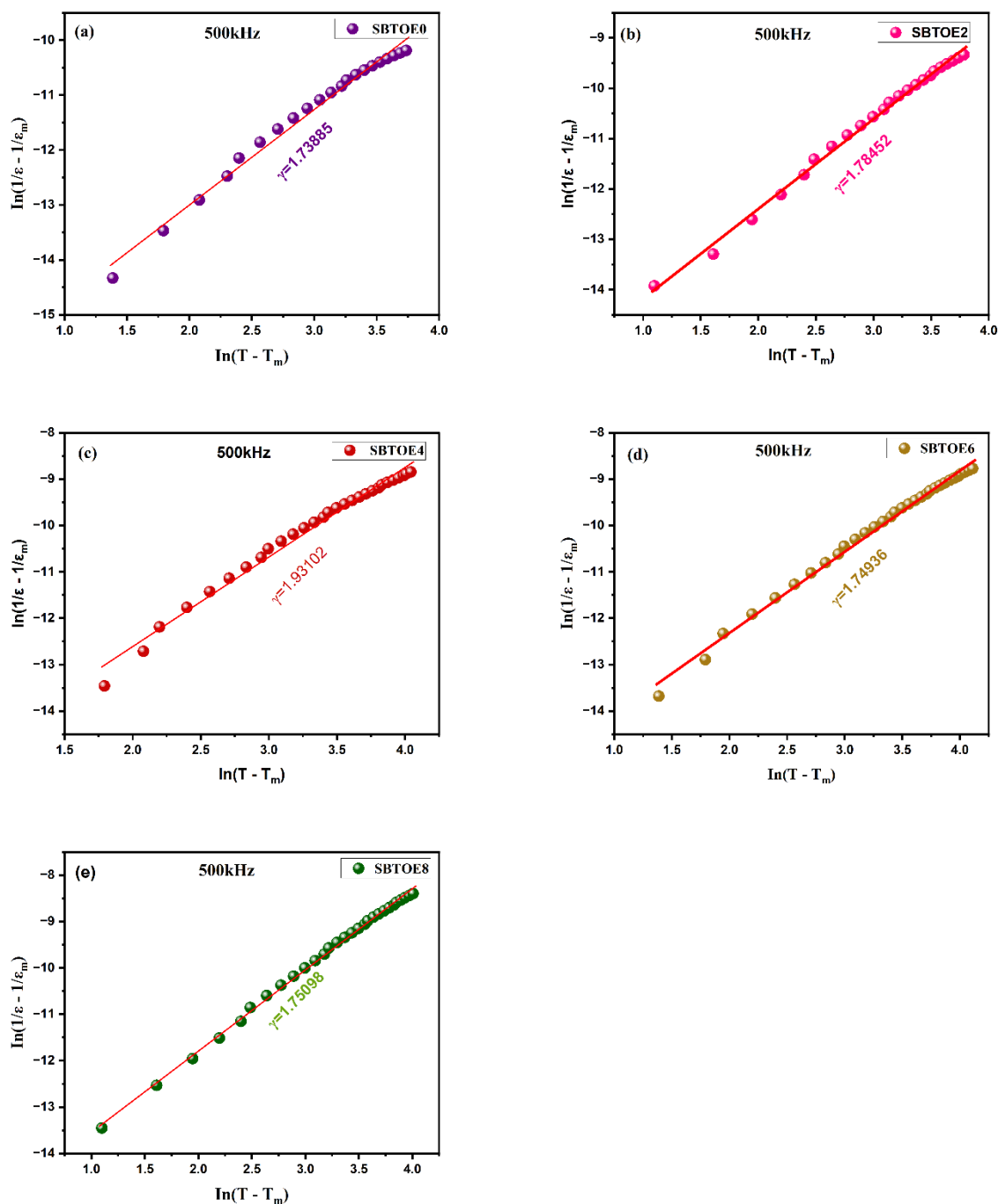
Fig.11. Diffuseness Behavior in $SrBi_2Ta_2O_9$:Er^{3+}: Modified Curie-Weiss Analysis of Phase Transition Broadening: (a) 0.00, (b) 0.02, (c) 0.04, (d) 0.06, (e) 0.08 Er^{3+} concentrations.
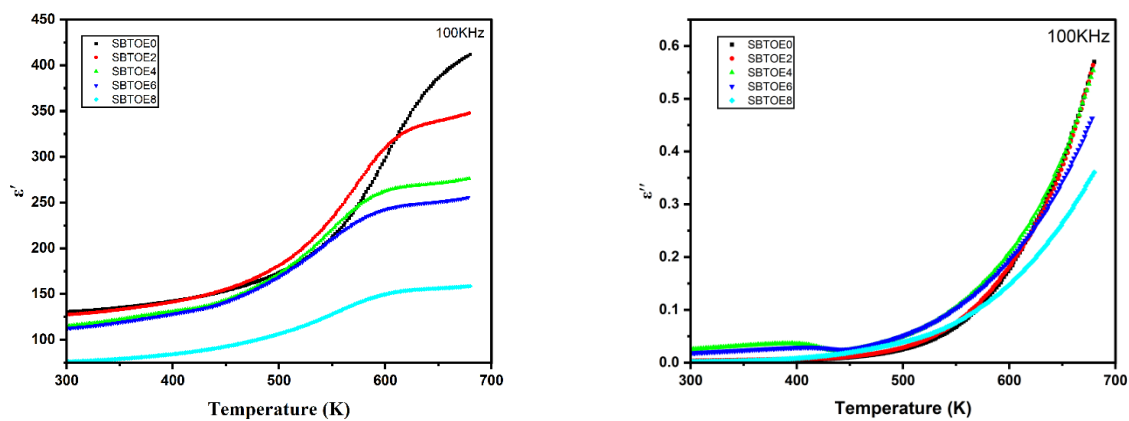
Fig.12. Concentration-Driven Reduction of dielectric constant (ε') and dielectric loss (ε'') in SrBi$_2$Ta$_2$O$_9$:Er^{3+} Ceramics

Polarization dynamics for high-efficiency energy storage and multifunctional memory solutions:

Ferroelectric materials exhibit unique polarization-electric field (P-E) hysteresis loops that are fundamental to understanding their behavior and applications in energy storage systems. This comprehensive analysis reveals that ferroelectric hysteresis loops demonstrate spontaneous polarization that can be reversed by external electric fields, creating characteristic butterfly-shaped curves with distinct energy storage and dissipation properties. The loop parameters including saturation polarization, remnant polarization, and coercive field directly determine energy storage capabilities, with recoverable energy densities reaching up to 14 J cm^{-3} in advanced materials while maintaining high efficiencies of 90% or greater. These remarkable properties position ferroelectric capacitors as essential components for next-generation energy storage applications requiring high power density, rapid charge-discharge cycles, and superior reliability.

A P-E hysteresis loop represents the relationship between electric polarization (P) and applied electric field (E) in ferroelectric materials. Ferroelectric materials exhibit spontaneous electric polarization that can be reversed by the application of an external electric field, analogous to ferromagnetic materials but with electrical rather than magnetic properties. The distinguishing feature of ferroelectrics is that the spontaneous polarization can be reversed by a suitably strong applied electric field in the opposite direction, making the polarization dependent not only on the current electric field but also on its history, yielding a hysteresis loop.

The hysteresis phenomenon occurs because ferroelectric materials retain their polarization state after being exposed to an electric field, making them useful as memories. This retention capability stems from the unique crystal structure of ferroelectric materials, where electric dipoles can adopt stable orientations that persist even when the external field is removed. When an electric field is applied, these dipoles align with the field direction, creating macroscopic polarization. Upon field reversal, the dipoles must overcome energy barriers to switch orientation, resulting in the characteristic hysteresis behavior.

Several critical parameters define the characteristics of P-E hysteresis loops. The saturation polarization (Ps) represents the maximum polarization achievable under high electric fields, typically occurring when all electric dipoles are aligned with the applied field. The remnant polarization (Pr) is the polarization remaining when the electric field returns to zero, indicating the material's ability to retain polarization without external stimulation. The coercive field (E_c) represents the electric field required to reduce polarization to zero, essentially the field needed to overcome the energy barriers for dipole switching.

Experimental measurements of these parameters require careful consideration of measurement techniques. The conventional approach evaluates remnant polarization at zero electric field and coercive field at zero polarization. However, due to the contribution from the linear dielectric component of ferroelectrics, direct evaluation can underestimate actual values. Advanced

modeling frameworks using Preisach models provide more accurate parameter extraction by accounting for the complex interactions between ferroelectric and dielectric contributions.

The relationship between these parameters reveals fundamental material properties. Research has shown systematic relationships where increasing coercive field correlates with decreasing polarization and dielectric constant, suggesting natural limits to material performance. These interdependencies guide material design strategies for optimizing specific applications.

Dielectric Capacitors and Energy Storage

Ferroelectric materials serve as essential components in high-performance energy storage capacitors due to their unique electrostatic energy storage mechanism. These capacitors demonstrate superior power density, ultrafast charge-discharge rates, and extended operational lifetimes compared to electrochemical alternatives. The high power density capabilities make ferroelectric capacitors indispensable for applications requiring rapid energy delivery, such as pulsed power systems and hybrid electric vehicles. The energy storage capabilities of ferroelectric capacitors enable miniaturization of electronic systems while maintaining performance requirements. Advanced applications include medical devices, military equipment, and next-generation automotive systems where space and weight constraints demand high energy density solutions.

Memory Applications and Data Storage

Ferroelectric hysteresis loops provide the fundamental basis for non-volatile memory applications. The bistable nature of ferroelectric polarization enables binary data storage, where different polarization states represent logic 0 and 1. Ferroelectric Random Access Memory (FeRAM) utilizes the remnant polarization to store data without continuous power, providing non-volatile storage with fast writing capabilities and low power consumption.

The memory applications exploit the switching charge during polarization reversal to detect stored information. When a switching voltage is applied during read operations, the resulting current indicates the initial polarization state. However, this read-out process is destructive, requiring reset operations to maintain data integrity. Advanced ferroelectric field-effect transistors (FeFET) offer non-destructive read-out capabilities but face challenges with retention times and material optimization.

Recent developments in ferroelectric memory technology focus on scaling miniaturization while maintaining performance. Ferroelectric properties persist down to several unit cells, making these materials attractive for nanoscale applications. However, reduced thickness introduces challenges from depolarizing fields and strain effects that must be carefully managed in device design.

Result and analysis:

The P-E hysteresis data and curves presented in Table.3. and Fig.13. for Er^{3+}-doped $SrBi_2Ta_2O_9$ (SBT) provide valuable insights into the material's energy storage properties and application potential. All measurements conducted at room temperature with an applied field range of 60 to 80 kV/cm and a frequency of 20 Hz. From table x we observed an increase in saturation polarization (Pm) from 1.74 µC/cm² (x=0.00) to 4.57 µC/cm² (x=0.04) at 80 kV/cm, followed by a decline to 2.52 µC/cm² (x=0.08). This behavior is attributed to Er^{3+} doping, which induces lattice distortion in the Aurivillius structure, enhancing TaO_6 octahedral tilting and Bi^{3+} off-centering [1]. At x=0.04, optimal doping maximizes polarization alignment. However, higher doping levels (x ≥ 0.06) introduce strain and defects, disrupting long-range dipole ordering. The Remnant Polarization (P_r) Rises from 0.145 µC/cm² (undoped) to 1.63 µC/cm² (x=0.04), Coercive Field (E_c) escalates from 5.68 kV/cm (undoped) to 16.4 kV/cm (x=0.04), reflecting increased energy required for polarization switching.

The P-E hysteresis loop provides direct access to energy calculations that are crucial for energy storage applications. The total energy density stored in a ferroelectric capacitor during charging is calculated by integrating the area under the charging curve from zero polarization to maximum polarization.

$$W_{total} = \int_0^{P_{max}} E \, dP$$

The recoverable energy (W_{rec}) density represents the useful energy that can be extracted from the capacitor during discharge. This quantity is calculated by integrating the area under the discharge curve from maximum polarization back to remnant polarization.

$$W_{rec} = \int_{P_r}^{P_{max}} E \, dP$$

And the energy efficiency (η) represents the ratio of recoverable energy to total energy input, providing a critical metric for practical applications.

$$\eta = \frac{W_{rec}}{W_{total}} \times 100$$

High energy efficiency indicates minimal energy loss during charge-discharge cycles, a crucial feature for practical energy storage systems. This efficiency depends on the hysteresis loop shape, with narrower loops correlating to lower hysteresis losses and improved efficiency. **Table.3.** lists the energy storage parameters (W, W_{rec} and η) for applied electric fields ranging from 60–80 kV/cm. These parameters tend to improve with increasing electric field, as illustrated in **Figure.14**. Our study demonstrates exceptional energy efficiencies across all concentrations, ranging from 65.6% to 96.8%. The energy storage performance of Er^{3+}-doped $SrBi_2Ta_2O_9$ (SBT) exhibits strong compositional dependence, with 2 mol% Er doping (x = 0.02) emerging as the optimal configuration at this concentration, the material achieves η = 95.3–96.8% across electric fields of

60–80 kV/cm, making it ideal for applications such as high-efficiency capacitors. In contrast, 4 mol% Er doping prioritizes polarization magnitude, achieving a high P_{max}= 4.57 μC/cm², though at the expense of efficiency (η = 65.6%). This positions the composition as ideal for moderate-efficiency systems where maximizing polarization density is critical.

Beyond energy storage, x=0.04 Er-SBT demonstrates exceptional potential for non-volatile ferroelectric memory (FeRAM). The elevated remnant polarization (P_r = 1.63 μC/cm²) enables stable binary data storage (logic 0/1), while the robust coercive field (E_c = 16.4 kV/cm) ensures long-term polarization retention critical for data integrity in harsh environments. The material's layered perovskite structure further enhances reliability. These dual functionalities high-efficiency energy storage and robust memory performance highlight the tunability of Er^{3+}-doped SBT, making it a versatile candidate for next-generation multifunctional electronic systems .

**Table.3.** Energy storage parameters of Er+3 doped SrBi2Ta2O9 ceramics for various concentration

Compositions	Parameters	Emax(kV/cm)				
		60kv	65kv	70kv	75kv	80KV
SBTOE0	Emax(kV/cm)	62.9989	62.33	73.59	79.16	84.77
	P_{max} (μC/cm²)	1.744	1.89	2.05	2.22	2.34
	W_{rev}(J/cm³)	46.88	56.5	65.4	77.2	88.25
	Wtotal(J/cm³)	55.74	64.76	75.59	87.25	100.17
	n(%)	84.10477	87.2452	86.5194	88.4814	88.1002
	Pr(μC/cm²)	0.145	0.181	0.173	0.19	0.206
	Ec(kV/cm)	5.684	5.42	5.54	5.798	5.964
SBTOE2	Emax(kV/cm)	60.353	65.889	71.317	76.861	85.286
	P_{max} (μC/cm²)	1.482	1.60125	1.761	1.907	2.121
	W_{rev}(J/cm³)	42.262	50.0655	59.052	69.608	85.376
	Wtotal(J/cm³)	44.335	51.6998	61.644	71.327	89.011
	n(%)	95.32424	96.8389	95.7952	97.59	95.9162
	Pr(μC/cm²)	0.059	0.053	0.065	0.08	0.089
	Ec(kV/cm)	2.303	2.602	2.568	2.668	3.845
SBTOE4	Emax(kV/cm)	60.7	71.16	72.05	77.28	82.34
	P_{max} (μC/cm²)	2.37	3	4.08	4.32	4.57
	W_{rev}(J/cm³)	58.86	82.91	85.8	97.76	110.96
	Wtotal(J/cm³)	71.61	104.62	131.99	148.9	167.6
	n(%)	82.19522	79.2487	65.0049	65.6548	66.2053
	Pr(μC/cm²)	0.341	0.525	1.515	1.573	1.63

	Ec(kV/cm)	6.8488	9.2757	15.3121	16.33	16.4
SBTOE6	Emax(kV/cm)	60.698	66.0395	71.433	77.178	82.7551
	P_{max} ($\mu C/cm^2$)	3.0788	3.3997	3.675	3.9963	4.2523
	$W_{rev}(J/cm^3)$	55.3838	65.68	75.54	87.66	99.82
	Wtotal(J/cm^3)	84.44	101.09	115.55	132.25	150
	n(%)	65.58953	64.9718	65.3743	66.2836	66.5467
	Pr($\mu C/cm^2$)	1.137	1.264	1.3823	1.5701	1.6357
	Ec(kV/cm)	13.2079	14.32	15.3825	15.997	16.9494
SBTOE8	Emax(kV/cm)	60.956	66.335	70.239	82.582	81.602
	P_{max} ($\mu C/cm^2$)	1.896	2.069	2.105	2.519	2.5161
	$W_{rev}(J/cm^3)$	44.448	51.098	59.878	80.87	78.532
	Wtotal(J/cm^3)	58.431	68.324	71.553	99.269	99.594
	n(%)	76.06921	74.7878	83.6834	81.4655	78.8521
	Pr($\mu C/cm^2$)	0.4046	0.4539	0.36244	0.4785	0.4856
	Ec(kV/cm)	11.098	11.4651	8.9248	12.0532	12.3686

36
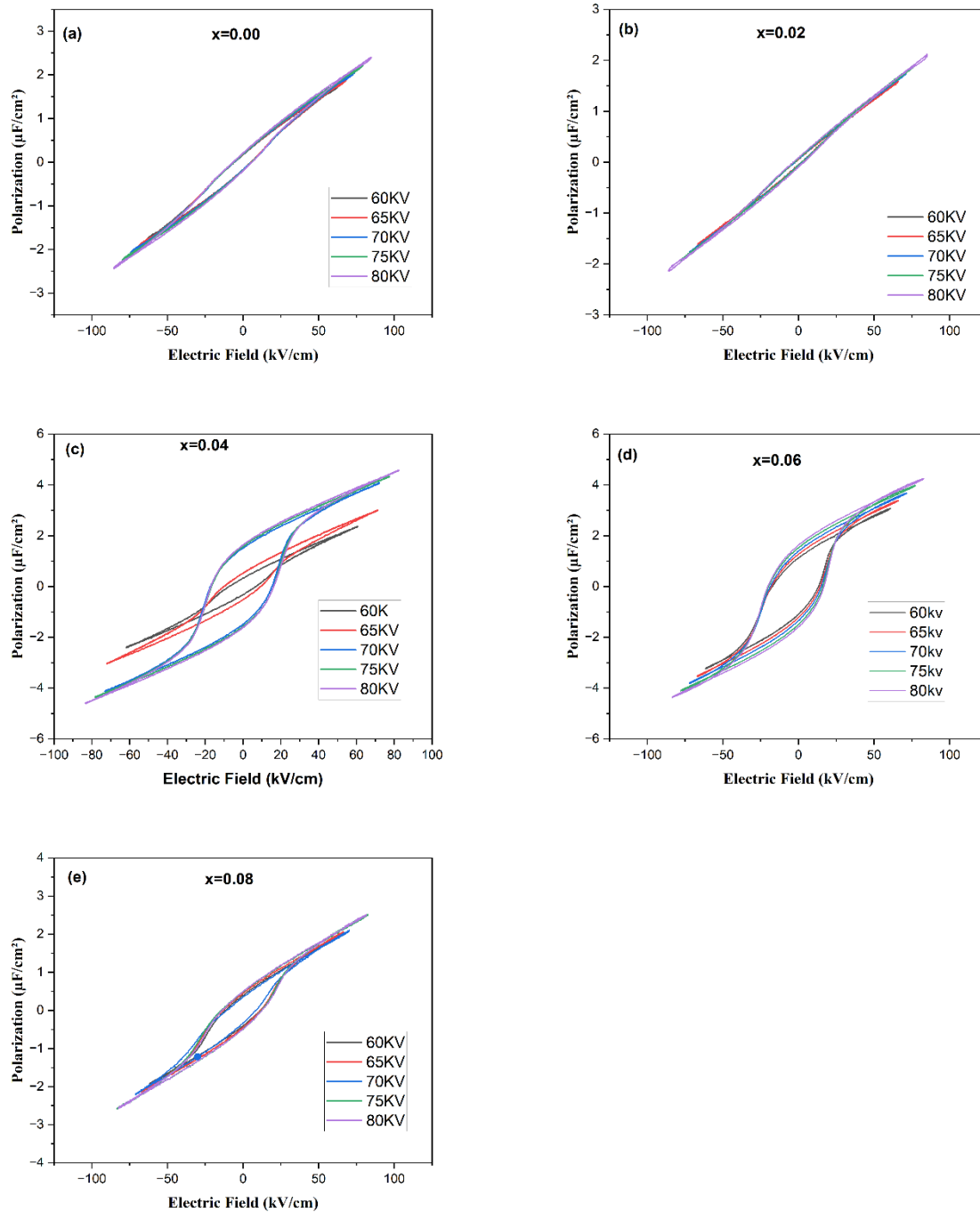
Fig.13. a-e P-E Loop Saturation Behavior in SrBi$_2$Ta$_2$O$_9$:Er^3 Ceramics for varying applied electric fields ranging from 60 to 80 kV/cm.
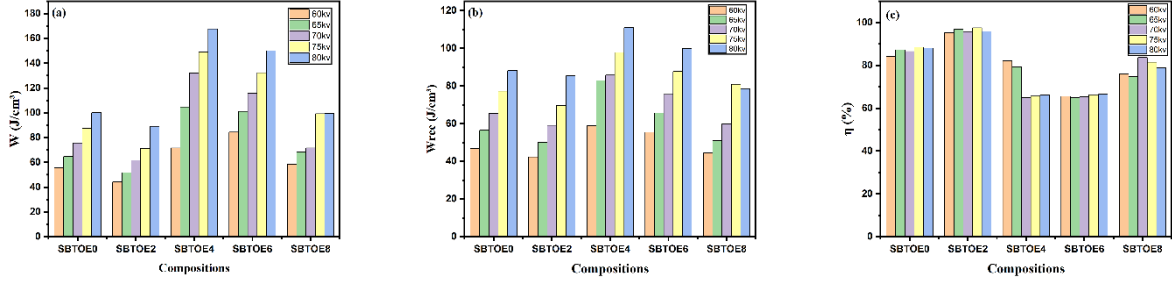
Fig.14. a–c Energy storage parameters of all the prepared compositions of BBN with varying applied electric fields ranging from 60 to 80 kV/ cm.

CHAPTER 5

Conclusion

This comprehensive study successfully demonstrates the systematic effects of Er^{3+} doping on $SrBi_2Ta_2O_9$ (SBT) ceramics across multiple concentration levels (x = 0.00-0.08), revealing critical structure-property relationships for next-generation multifunctional electronic materials. The research confirms complete Er^{3+} incorporation into the Aurivillius host structure while preserving phase purity, with optimal doping concentrations emerging for distinct applications: x = 0.04 for maximum photoluminescence intensity and ferroelectric polarization (4.57 $\mu C/cm^2$), and x = 0.02 for superior energy storage efficiency (95.3-96.8%). The investigation reveals that Er^{3+} substitution at Bi^{3+} sites induces controlled lattice distortion, enhancing both green upconversion emission and ferroelectric properties while introducing relaxor-like behavior at critical doping levels.

Structural and Morphological Characteristics

X-ray diffraction analysis confirmed the successful synthesis of single-phase orthorhombic $SrBi_{2-x}Er_xTa_2O_9$ ceramics with complete Er^{3+} incorporation into the host lattice structure1. The systematic investigation revealed that Er^{3+} substitution at Bi^{3+} sites introduces controlled lattice distortion, evidenced by changes in lattice parameters and the b/a ratio with increasing erbium concentration. Scanning electron microscopy demonstrated that particle morphology follows the characteristic plate-like structure typical of bismuth layer structured ferroelectrics, with average particle size reaching an optimal value of 1.98 μm at x = 0.04, which directly correlates with the observed maximum luminescence intensity. This size optimization reflects the balance between Er^{3+} integration efficiency and crystalline quality, where moderate doping levels enhance structural ordering while excessive concentrations introduce lattice strain and defects that limit both optical and electrical performance.

The density measurements revealed a systematic decrease with increasing Er^{3+} content, attributed to the smaller ionic radius of Er^{3+} ($\approx$1.00 Å) compared to Bi^{3+} ($\approx$1.17 Å), confirming successful substitution while maintaining structural integrity1. Fourier-transform infrared spectroscopy analysis verified the preservation of the fundamental Aurivillius structure across all doping concentrations, with systematic broadening and frequency shifts in the Ta-O stretching modes around 600-650 cm^{-1} indicating successful Er^{3+} incorporation and resulting octahedral distortion.

Optical Properties and Photoluminescence Behavior

The photoluminescence investigation revealed strong green upconversion emission under 488 nm excitation, with two prominent peaks at 524 nm and 549 nm corresponding to $^2H_{11/2} \rightarrow {}^4I_{15/2}$ and $^4S_{3/2} \rightarrow {}^4I_{15/2}$ transitions, respectively. The emission intensity exhibited concentration-dependent behavior, reaching maximum values at x = 0.04 before experiencing concentration quenching at higher doping levels due to enhanced non-radiative energy transfer between closely spaced Er^{3+}

ions1. The diffuse reflectance spectroscopy analysis identified multiple absorption bands corresponding to f-f electronic transitions from the ground state $^4I_{15/2}$ to various excited states of Er^{3+}, with optical band gap values ranging from 2.74 to 3.46 eV across the doping series1. Notably, the emission wavelengths remained stable across all doping concentrations, indicating that the crystal field environment provides consistent optical properties while allowing intensity modulation through concentration control.

The upconversion mechanism analysis confirmed efficient energy transfer processes within the Er^{3+}-doped SBT matrix, with the layered perovskite structure providing an optimal host environment for rare earth luminescence. The observed green emission dominance over red emission in lower doping concentrations reflects the energy level structure and phonon-assisted relaxation pathways specific to the Aurivillius host, making these materials particularly suitable for green phosphor applications in photonic devices.

Dielectric and Ferroelectric Properties

Comprehensive dielectric characterization revealed frequency-dependent behavior characteristic of relaxor ferroelectric materials, with dielectric constants decreasing systematically with increasing frequency across all compositions. The introduction of Er^{3+} doping significantly influenced the ferroelectric-to-paraelectric phase transition, with the diffuseness parameter (γ) reaching a maximum value of 1.93102 at x = 0.04, approaching the theoretical limit for complete relaxor behavior ($\gamma = 2$). This critical concentration represents a crossover point where the material exhibits optimal relaxor characteristics while maintaining substantial ferroelectric properties. The temperature-dependent dielectric measurements demonstrated that Er^{3+} substitution effectively reduces dielectric loss through domain wall pinning mechanisms while modulating the Curie temperature, creating opportunities for temperature-stable applications.

The systematic reduction in maximum dielectric constant from approximately 1000 (undoped) to 600 (x = 0.04) reflects the Er^{3+}-induced structural inhomogeneity and weakened dipolar ordering, which paradoxically enhances the material's suitability for specific electronic applications requiring controlled dielectric response1. The frequency dispersion analysis confirmed that dipolar relaxation becomes the primary loss mechanism at higher frequencies, with all doped compositions showing improved high-frequency stability compared to the undoped reference material.

Energy Storage and Memory Applications

The polarization-electric field hysteresis measurements revealed exceptional energy storage capabilities, with energy efficiency values ranging from 65.6% to 96.8% across different doping concentrations and applied electric fields1. The composition with x = 0.02 emerged as optimal for energy storage applications, achieving remarkable efficiency values of 95.3-96.8% across electric fields of 60-80 kV/cm, positioning it as an ideal candidate for high-efficiency capacitor applications. In contrast, the x = 0.04 composition demonstrated superior polarization magnitude

(P_{max} = 4.57 $\mu C/cm^2$) with moderate efficiency (η = 65.6%), making it particularly suitable for applications where maximizing polarization density is critical.

The ferroelectric memory potential was particularly evident in the x = 0.04 composition, which exhibited elevated remnant polarization (P_r = 1.63 $\mu C/cm^2$) and robust coercive field (E^c = 16.4 kV/cm), ensuring stable binary data storage and long-term polarization retention essential for non-volatile ferroelectric random access memory (FeRAM) applications. The dual functionality observed in Er^{3+}-doped SBT combining high-efficiency energy storage with robust memory performance highlights the material's versatility for next-generation multifunctional electronic systems.

This systematic investigation successfully demonstrates that Er^{3+} doping provides precise control over the multifunctional properties of $SrBi_2Ta_2O_9$ ceramics, enabling optimization for distinct technological applications through compositional engineering. The research reveals that x = 0.02 represents the optimal composition for high-efficiency energy storage applications with exceptional efficiency values of 95.3-96.8%, while x = 0.04 emerges as the ideal concentration for maximizing both photoluminescence intensity and ferroelectric polarization, positioning these materials as promising candidates for integrated optoelectronic systems1. The observed concentration-dependent transition from normal ferroelectric to relaxor-like behavior, coupled with bright green upconversion emission, establishes Er^{3+}-doped SBT as a versatile platform for multifunctional device architectures.

While this study comprehensively characterizes the fundamental properties across a specific doping range, future investigations should explore the optimization of processing parameters to further enhance properties, investigate the effects of alternative rare earth dopants for comparison, and develop prototype devices to validate the practical applications of these multifunctional ceramics. The demonstrated dual functionality combining efficient energy storage, stable memory performance, and bright upconversion luminescence positions Er^{3+}-doped $SrBi_2Ta_2O_9$ ceramics as transformative materials for next-generation electronics, where device miniaturization and functional integration are paramount for advancing sustainable and efficient technological solutions.

CHAPTER 7

Bibliography

[1]   H. Nagata, S. Horiuchi, Y. Hiruma, and T. Takenaka, "Bismuth layer-structured ferroelectric (Sr, Ca) 2 Bi 4 Ti 5 O 18 ceramics for lead-free piezoelectric resonator applications," 2005.

[2]   R. Bokolia, O. P. Thakur, V. K. Rai, S. K. Sharma, and K. Sreenivas, "Dielectric, ferroelectric and photoluminescence properties of Er3+ doped Bi4Ti3O12 ferroelectric ceramics," *Ceram Int*, vol. 41, no. 4, pp. 6055–6066, May 2015, doi: 10.1016/j.ceramint.2015.01.062.

[3]   A. Shandilya, R. S. Yadav, A. K. Gupta, and K. Sreenivas, "Effects of Yb3+ ion doping on lattice distortion, optical absorption and light upconversion in Er3+/Yb3+ co-doped SrMoO4 ceramics," *Mater Chem Phys*, vol. 264, May 2021, doi: 10.1016/j.matchemphys.2021.124441.

[4]   F. Wang *et al.*, "Simultaneous phase and size control of upconversion nanocrystals through lanthanide doping," *Nature*, vol. 463, no. 7284, pp. 1061–1065, Feb. 2010, doi: 10.1038/NATURE08777;SUBJMETA=1020,301,354,357,537,624,639;KWRD=LASERS.

[5]   M. P. Moret, R. Zallen, R. E. Newnham, P. C. Joshi, and S. B. Desu, "Infrared activity in the Aurivillius layered ferroelectric SrBi 2 Ta 2 O 9," 1998.

[6]   M. Afqir *et al.*, "Synthesis, structural and dielectric properties of SrBi 2 Ta 2 O 9 prepared via co-precipitation method," 2016. [Online]. Available: http://www.ijias.issr-journals.org/

[7]   A. Banwal and R. Bokolia, "Preparation and characterisations of Yb3+ substituted BaBi2-yNb2YbyO9 ferroelectric ceramic," *Mater Today Proc*, vol. 62, pp. 3782–3785, Jan. 2022, doi: 10.1016/J.MATPR.2022.04.459.

[8]   A. Banwal and R. Bokolia, "Effect of Er3+ ion doping on structural, ferroelectric and up/down conversion luminescence in BaBi2Nb2O9 ceramic," *Mater Today Proc*, vol. 47, pp. 4692–4695, Jan. 2021, doi: 10.1016/J.MATPR.2021.05.545.

[9]   A. Banwal, R. B.-M. T. Proceedings, and undefined 2021, "Phase evolution and microstructure of BaBi2Nb2O9 ferroelectric ceramics," *ElsevierA Banwal, R BokoliaMaterials Today: Proceedings, 2021•Elsevier*, Accessed: Jun. 07, 2025. [Online]. Available: https://www.sciencedirect.com/science/article/pii/S2214785320370966

[10]   A. Banwal and R. Bokolia, "Efficient tunable temperature sensitivity in thermally coupled levels of Er3+/Yb3+ co-doped BaBi2Nb2O9 ferroelectric ceramic," *J Lumin*, vol. 263, p. 120071, Nov. 2023, doi: 10.1016/J.JLUMIN.2023.120071.

[11]   A. Banwal, R. B.-C. International, and undefined 2022, "Enhanced upconversion luminescence and optical temperature sensing performance in Er3+ doped BaBi2Nb2O9 ferroelectric ceramic," *ElsevierA Banwal, R BokoliaCeramics International, 2022•Elsevier*, Accessed: Jun. 07, 2025. [Online]. Available: https://www.sciencedirect.com/science/article/pii/S0272884221031242

[12]   M. Narwan, A. Banwal, R. Sharma, and R. Bokolia, "Non-invasive thermal sensing and improved recoverable energy storage density of Bi0.5Na0.5TiO3: Er3+ doped multifunctional ferroelectric ceramic," *J Lumin*, vol. 265, p. 120236, Jan. 2024, doi: 10.1016/J.JLUMIN.2023.120236.

[13]   J. Liao *et al.*, "Effect of Yb3+ concentration on tunable upconversion luminescence and optically temperature sensing behavior in Gd2TiO5:Yb3+/Er3+phosphors," *Opt Mater (Amst)*, vol. 75, pp. 841–849, Jan. 2018, doi: 10.1016/J.OPTMAT.2017.12.009.

[14]   M. Gupta, M. Adnan, R. Nagarajan, and G. Vijaya Prakash, "Color-Tunable Upconversion in Er3+/Yb3+-Codoped KLaF4 Nanophosphors by Incorporation of Tm3+ Ions for Biological Applications," *ACS Omega*, vol. 4, no. 1, pp. 2275–2282, Jan. 2019, doi: 10.1021/ACSOMEGA.8B03075/ASSET/IMAGES/LARGE/AO-2018-03075A_0005.JPEG.

[15]   A. Kurakula *et al.*, "Aurivillius-Type SrBi4Ti4O15/PGA Composite Film-Based Flexible Triboelectric Nanogenerators for Energy Harvesting/Storage and Multipurpose Tap-Indication Transducer Applications," *ACS Appl Mater Interfaces*, vol. 16, no. 36, pp. 48246–48256, Sep. 2024, doi: 10.1021/ACSAMI.4C09183/SUPPL_FILE/AM4C09183_SI_004.MP4.

[16]   A. Enachi, O. Toma, and Ş. Georgescu, "Luminescent Er3+ centers in CaSc2O4:Er3+:Yb3+ upconversion phosphor," *J Lumin*, vol. 231, p. 117816, Mar. 2021, doi: 10.1016/J.JLUMIN.2020.117816.

[17]   Y. Zhang, R. Chu, Z. Xu, S. Zhang, C. Zhang, and G. Li, "Electrical and luminescence properties, and energy band structure of SrBi2-xErxNb2O9 multifunctional ceramics," *Ceram Int*, vol. 47, no. 21, pp. 30938–30946, Nov. 2021, doi: 10.1016/J.CERAMINT.2021.07.279.

[18]   11 Tb+3 and Y. W. T. C. 4ll2, "THE NEAR-INFRARED TRANSITIONS OF THE TRIVALENT LANTHANIDES I N SOLUTION."

[19]   P. Rohilla and A. S. Rao, "Synthesis optimisation and efficiency enhancement in Eu3+ doped barium molybdenum titanate phosphors for w-LED applications," *Mater Res Bull*, vol. 150, p. 111753, Jun. 2022, doi: 10.1016/J.MATERRESBULL.2022.111753.

[20]   L. Wang *et al.*, "Dual-Mode Luminescence with Broad Near UV and Blue Excitation Band from Sr2CaMoO6:Sm3+ Phosphor for White LEDs," *Journal of Physical Chemistry C*, vol. 119, no. 27, pp. 15517–15525, Jul. 2015, doi: 10.1021/ACS.JPCC.5B02828/ASSET/IMAGES/MEDIUM/JP-2015-02828D_0011.GIF.

[21]   P. C. Joshi, S. O. Ryu, X. Zhang, and S. B. Desu, "Properties of SrBi2Ta2O9 ferroelectric thin films prepared by a modified metalorganic solution deposition technique," *Appl Phys Lett*, vol. 70, no. 9, pp. 1080–1082, Mar. 1997, doi: 10.1063/1.118485.

[22]   F. Kadlec, S. Kamba, P. Kužel, C. Kadlec, and J. Kroupa, "High-temperature THz dielectric spectra of SrBi 2 Ta 2 O 9 thick film."

[23]   Y. Wu, M. J. Forbess, S. Seraji, S. J. Limmer, T. P. Chou, and G. Cao, "Impedance study of SrBi 2 Ta 2 O 9 and SrBi 2 (Ta 0. 9 V 0. 1) 2 O 9 ferroelectrics," 2001. [Online]. Available: www.elsevier.com/locate/mseb

[24]   R. Machado, M. Sepliarsky, and M. G. Stachiotti, "Temperature-driven phase transitions in SrBi 2 Ta 2 O 9 from first-principles calculations."

[25]   S. Mitra, A. R. Kulkarni, and O. Prakash, "Diffuse phase transition and electrical properties of lead-free piezoelectric (Li x Na 1-x)NbO 3 (0.04 ≤ x ≤ 0.20) ceramics near morphotropic phase boundary."

[26]   R. D. ' Souza, "SYNTHESIS AND CHARACTERISATION OF MATERIALS WITH POTENTIAL MULTIFERROIC BEHAVIOUR," 2008.

[27]   M. Z. Amin, K. K. Qureshi, and M. M. Hossain, "Doping Radius Effects on Erbium Doped Fiber Amplifier (EDFA)."

[28]   F. Liu *et al.*, "Structural, electrical and photoluminescence properties of Er 3+ -doped SrBi 4 Ti 4 O 15 —Bi 4 Ti 3 O 12 inter-growth ceramics," *Front Mater Sci*, vol. 13, no. 1, pp. 99–106, Mar. 2019, doi: 10.1007/s11706-019-0454-3.

[29]   C. Rayssi, S. El Kossi, J. Dhahri, and K. Khirouni, "Frequency and temperature-dependence of dielectric permittivity and electric modulus studies of the solid solution

Ca0.85Er0.1Ti1-: XCo4 x /3O3 (0 ≤ x ≤ 0.1)," *RSC Adv*, vol. 8, no. 31, pp. 17139–17150, 2018, doi: 10.1039/c8ra00794b.

[30]   C. C. Wu and C. F. Yang, "Effect of V2O5 B-site substitution on the microstructure, Raman spectrum, and dielectric properties of SrBi2Ta2O9 ceramics," *Sci Rep*, vol. 10, no. 1, Dec. 2020, doi: 10.1038/s41598-020-73327-2.

[31]   M. Afqir *et al.*, "Structure and dielectric properties of Lu-doped SrBi2Ta2O9 synthesized by the molten salt method," *Processing and Application of Ceramics*, vol. 17, no. 3, pp. 256–263, 2023, doi: 10.2298/PAC2303256A.

[32]   C. C. Wu and C. F. Yang, "Relationship between Crystal Structures and the Relaxor Property of SrBi2(Ta2-xVx)O9 Ceramics," *ACS Omega*, vol. 4, no. 17, pp. 17125–17133, Oct. 2019, doi: 10.1021/acsomega.9b01398.

[33]   K. Saenkam, P. Jaita, S. Sirisoonthorn, T. Tunkasiri, and G. Rujijangul, "Effects of processing parameter on energy storage density and ferroelectric properties of lead-free bismuth sodium titanate-strontium bismuth titanate ceramics," *ScienceAsia*, vol. 47, no. S1, pp. 34–41, Jul. 2021, doi: 10.2306/SCIENCEASIA1513-1874.2021.S005.

[34]   "Formation and Characterization of SrBi 2 Ta 2 O 9 (SBT) Thin Film Capacitor Module with Platinum/Titanium Bottom and Platinum Top Electrodes."

[35]   J. Mun *et al.*, "Probing ferroelectric domain structures and their switching dynamics in SrBi2Ta2O9 by in-situ electric biasing in transmission electron microscopy," *Commun Mater*, vol. 5, no. 1, Dec. 2024, doi: 10.1038/s43246-024-00593-2.

CHAPTER 8

Plagiarism report

MSC THESIS 1 .docx

Delhi Technological University

Document Details

Submission ID
trn:oid:::27535:99821655

Submission Date
Jun 8, 2025, 10:27 AM GMT+5:30

Download Date
Jun 8, 2025, 10:29 AM GMT+5:30

File Name
MSC THESIS 1 .docx

File Size
3.2 MB

43 Pages

8,999 Words

58,945 Characters

2% Overall Similarity

The combined total of all matches, including overlapping sources, for each database.

Filtered from the Report

- ▸ Bibliography
- ▸ Quoted Text
- ▸ Cited Text
- ▸ Small Matches (less than 12 words)

Match Groups

🔴 **14** Not Cited or Quoted 2%
Matches with neither in-text citation nor quotation marks

🟠 **0** Missing Quotations 0%
Matches that are still very similar to source material

🟡 **0** Missing Citation 0%
Matches that have quotation marks, but no in-text citation

🔵 **0** Cited and Quoted 0%
Matches with in-text citation present, but no quotation marks

Top Sources

1% 🌐 Internet sources

0% 📖 Publications

1% 👤 Submitted works (Student Papers)

Integrity Flags

1 Integrity Flag for Review

🚩 **Replaced Characters**
15 suspect characters on 16 pages
Letters are swapped with similar characters from another alphabet.

> Our system's algorithms look deeply at a document for any inconsistencies that would set it apart from a normal submission. If we notice something strange, we flag it for you to review.
>
> A Flag is not necessarily an indicator of a problem. However, we'd recommend you focus your attention there for further review.

Match Groups

🔴 **14** Not Cited or Quoted 2%
   Matches with neither in-text citation nor quotation marks

💬 **0** Missing Quotations 0%
   Matches that are still very similar to source material

🟰 **0** Missing Citation 0%
   Matches that have quotation marks, but no in-text citation

🔖 **0** Cited and Quoted 0%
   Matches with in-text citation present, but no quotation marks

Top Sources

1%	🌐	Internet sources
0%	📖	Publications
1%	👤	Submitted works (Student Papers)

Top Sources

The sources with the highest number of matches within the submission. Overlapping sources will not be displayed.

1 Submitted works
AlHussein Technical University on 2025-01-26   <1%

2 Submitted works
University of Witwatersrand on 2024-03-24   <1%

3 Internet
cicy.repositorioinstitucional.mx   <1%

4 Submitted works
The Open University of Hong Kong on 2025-04-18   <1%

5 Submitted works
Indian Institute of Engineering Science and Technology on 2022-12-26   <1%

6 Submitted works
University of Dundee on 2019-12-15   <1%

7 Publication
Yanxi Chen, Fanyun Su, Yuqing Rang, Guangli Liu, Xinxing Xu, Yayun Ma, Jingjing ...   <1%

8 Internet
www.researchgate.net   <1%

9 Publication
Feihong Pang, Xiu Li Chen, Congcong Sun, Junpeng Shi, Xu Li, Hongyun Chen, Xia...   <1%

10 Submitted works
University of Newcastle on 2024-11-03   <1%

CHAPTER 9

Conference Record

Proof of Registration

RAM 2024
Second International Conference on Recent Trends in Applied Physics & Material Science

Nov. 15-16, 2024
Bikaner, India
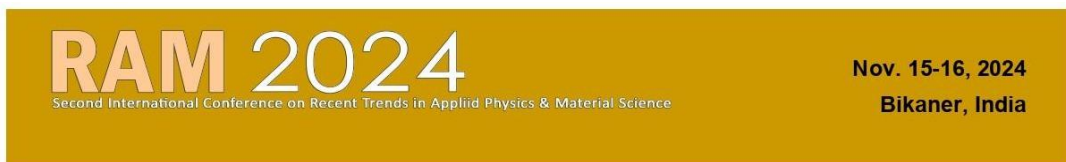
Payment Receipt

Receipt No : **RAM00188**   Date :   **2024-10-15 10:14:32**

Received with thanks from   **Mr. Vyom Khare [Postgraduate Student]**
Delhi Technological University

The sum of rupees   **Four Thousand Only**

for   **Registration Fee - V4-Research Scholar**

Papers   **-L1-0012**

Transaction ID : **428982275682**	Transaction Type : **BHIM UPI**
Bank Ref No : **-**	Bank ID : **---**
Surcharge : **-**	Total Amount : **4000.00**

Thanks,

Dr. Sudhir Bhardwaj

Organizing Secretary, RAM-2024
Bikaner Technical University,
Bikaner - 334001
Rajasthan, INDIA.
www.ramindia.in

Dr. Sudhir Bhardwaj,   Organizing Secretary, RAM-2024
Bikaner Technical University, RIICO Karni Industrial Area, Pugal Road,
Bikaner-334001 (Rajasthan) India

Mobile : +91-9468764401, E-mail : convener@ramindia.in
Website: www.ramindia.in

Certificate of participation

RAM 2024

Second International Conference
on Recent Trends in Applied Physics & Material Science

Paper ID : L1-0012

Certificate

This is to certify that
Mr. Vyom Khare
of
Delhi Technological University

has participated in Second International Conference on
Recent Trends in Appiled Physics & Material Science
(RAM 2024) organized by
Bikaner Technical University, Bikaner in joint auspices of
Condensed Matter Research Society
during Nov. 15-16, 2024 and presented a paper entitled
Structural and photoluminescence properties of Er3+ doped SrBi2Ta2O9 ceramics

Dr. Bhuvneshwer Suthar
Convener, RAM 2024
Govt. Dungar College, Bikaner

Dr. Manoj S. Shekhawat
Joint Secretary, RAM 2024
Govt. Engineering College, Bikaner

Dr. Sudhir Bhardwaj
Organizing Secretary, RAM 2024
Bikaner Technical University, Bikaner

www.ramindia.in

15-16 Nov, 2024 @ Bikaner

50

Second International Conference
on Recent Trends in Applied Physics & Material Science

Paper ID : L1-0012

Certificate

This is to certify that

Mr. Devesh Garg

of

Delhi Technological University

has participated in Second International Conference on
Recent Trends in Appiled Physics & Material Science
(RAM 2024) organized by
Bikaner Technical University, Bikaner in joint auspices of
Condensed Matter Research Society
during Nov. 15-16, 2024 and presented a paper entitled
Structural and photoluminescence properties of Er3+ doped SrBi2Ta2O9 ceramics

Dr. Bhuvneshwer Suthar
Convener, RAM 2024
Govt. Dungar College, Bikaner

Dr. Manoj S. Shekhawat
Joint Secretary, RAM 2024
Govt. Engineering College, Bikaner

Dr. Sudhir Bhardwaj
Organizing Secretary, RAM 2024
Bikaner Technical University, Bikaner

www.ramindia.in

15-16 Nov, 2024 @ Bikaner

Proof of acceptance

M Gmail

vyom khare <vyomkhare11@gmail.com>

RAM 2024 Paper Response
1 message

RAM 2024 Paper Response <info@ramindia.in>   Mon, Mar 24, 2025 at 10:02 PM
Reply-To: Reply <info@ramindia.in>
To: vyomkhare11@gmail.com

RAM 2024   **Second International Conference** on Recent Trends in
Applied Physics & Material Science

Dear Vyom Khare,

As per recommendation of review committee, we are glad to inform you that your paper as per following details submitted to RAM 2024 has been accepted for publication in Conference Proceedings CRC Press (part of Taylor & Francis Group).

Paper No: L1-0012
Title: Structural and photoluminescence properties of Er^{3+} doped $SrBi_2Ta_2O_9$ ceramics
Authors: Vyom Khare

Your paper will be published in Conference Proceedings CRC Press (part of Taylor & Francis Group). Now, the following process has to complete within one week after acceptance.
(1) The duly filled copyright form for your paper will be uploaded in login account of conference website. The copyright form may be downloaded from conference website Click here and fill the title of paper, authors name, Name and signature of corresponding author with date.
(2) If your paper contains more than two pages, you must pay Rs. 1500/- per extra page and provide confirmation of the payment.

Regards,

Dr. Bhuvneshwar Suthar
Convener, RAM 2024
Govt. Dungar College, Jaipur Road,
Bikaner (Rajasthan) India -334001
Mobile : +91-7014785025

Please do not reply to this system generated email. If you need any more information, please write to us at E-mail: convener@ramindia.in

Scopus Indexing

RAM 2024 | Home | About ⌄ | Call for Papers | Speakers | Committee ⌄ | Conference ⌄ | Downloads | Contact Us | **Register Now**

Conference Publication

The abstract is only required to submit for the presentation of your work in RAM 2024. Abstact Book of RAM 2024 will be published with ISBN number.

Login

The presented papers of the conference may be submitted for the publication with the following options as

CRC Press Taylor & Francis Group

Conference Proceedings with Taylor & Francis with ISBN (2 printed pages*)

All the submitted papers for RAM2024 will undergo the review process by the Review Committee. The conference proceeding of RAM 2024 will be published by CRC Press, Taylor & Francis Group. **The proceeding (after publication) will be submitted to SCOPUS by CRC Press, Taylor & Francis Group.**

Published paper

110

Structural and Photoluminescence Properties of Er^{3+} Doped SrBi$_2$Ta$_2$O$_9$ Ceramics

**Vyom Khare*, Devesh Garg, Megha Narwan,
Surya Pratap Singh, Renuka Bokolia**

Functional Materials Research Laboratory (FMRL),
Delhi Technological University (DTU), New Delhi, India

Abstract: This research investigated the structural and luminescent properties of Er^{3+}-doped SrBi$_2$Ta$_2$O$_9$ ceramic materials. The ceramic samples were fabricated using conventional solid-state reaction method. Variations in the dopant concentration (x = 0.00, 0.02, 0.04) were explored to assess their impact on its luminescence and structural characteristics. X-ray diffraction techniques were employed to confirm that the samples had a single-phase orthorhombic structure with space group A21am after heat treatment that included calcination at 900°C and sintering in the 1050°C temperature range. The SEM images shows a microstructure featuring grains of varying sizes that are randomly oriented, accompanied by noticeable porosity in the sintered pellets. Furthermore, the photoluminescence (PL) spectra were studied at specific excitation wavelengths of 488nm, highlighting the enhanced luminescent properties attributed to Er^{3+} doping. This research underscores the potential of rare-earth-doped ferroelectric ceramics in various energy-related applications, including optoelectronics and sensing technologies.

Keywords: ##

▶ 1. INTRODUCTION

Recent researches has highlighted the significance of photoluminescence in rare-earth-doped materials, as these materials have diverse applications in energy-related fields including temperature sensing, Lighting, display technologies, solar cells and biomedical applications.

Ferroelectric materials are characterized to display the spontaneous polarization that can be reversed under an external electric field. Their unique properties include high dielectric constants, fatigue resistance, high Curie temperatures, and notable piezoelectric effects, make them suitable for various energy-related applications, including optoelectronics and sensing technologies[1]. Among these materials, Bismuth-layered structure ferroelectrics (BLSFs), particularly from the Aurivillius

family, are attracting significant interest. These materials are represented by the formula $(Bi_2O_2)^{2+}(A_{n-1}B_nO_{3n+1})^2$. A notable example is SrBi$_2$Ta$_2$O$_9$ (SBT), which is lead-free and features a high Curie temperature of 600 K along with low dielectric loss. Doping materials like SrBi$_2$Ta$_2$O$_9$ with rare-earth ions such as Er^{3+}, Eu^{3+}, and Pr^{3+} has been shown to improve both their electrical and luminescent properties. This study aims to synthesize Er^{3+}-doped SrBi$_2$Ta$_2$O$_9$ ceramics using traditional solid-state methods and investigate how this doping influences their crystal structures and luminescent characteristics.

▶ 2. SYNTHESIS OF MATERIAL

In this study, polycrystalline ceramics of Er^{3+}-doped SrBi$_{2-x}$Ta$_2$Er$_x$O$_9$ with (x= 0.00, 0.02, 0.04) were prepared

*Corresponding author: vyomkhare18@gmail.com

using a conventional solid-state reaction method. It began with the precise weighing of high-purity starting materials: Tantalum oxide (Ta$_2$O$_5$), Strontium carbonate (SrCO$_3$), Bismuth oxide (Bi$_2$O$_3$), and Erbium oxide (Er$_2$O$_3$). These materials were mixed in their stoichiometric ratios and ground together using a mortar and pestle with ethanol added to aid the process, continuing until the mixture was dry; this grinding was performed for six hours to ensure uniformity. The resulting powders were calcined at 900 °C for three hours to facilitate solid-state reactions and improve material properties. After calcination, a binder solution consisting of 5 wt% PVA was added to the powders and mixed thoroughly. Disk-shaped pellets were then formed using a hydraulic press operated manually at a pressure of 50 MPa. Finally, the pellets were sintered at 1050 °C for three hours to ensure that the final ceramic structure was free from organic residues, optimizing their electrical and luminescent properties.[2], [3]

3. CHARACTERIZATION DETAILS

X-ray diffraction techniques were employed to study the phase and crystal structure of SrBi$_{2-x}$Ta$_2$Er$_x$O$_9$ sintered pallets. The XRD patterns were acquired using a Bruker D8 Discover X-ray diffractometer. This approach enabled the identification of the crystalline phases present in the samples and offered insights about their structural properties. To further examine the structural morphology of SrBi2$_{-x}$Ta$_2$Er$_x$O$_9$, unpolished sintered pellets were analyzed using scanning electron microscopy. The analysis was conducted using JEOL JSM 6610LV, enabling a comprehensive assessment of the surface morphology. Additionally, the photoluminescence (PL) properties of the Er^{3+}-doped SrBi$_2$Ta$_2$O$_9$ ceramics were assessed by recording PL spectra using an excitation wavelength of λ_{ex}=488 nm. This measurement provided valuable information regarding the luminescent behavior of the doped materials, highlighting their potential applications in optoelectronic devices.

4. RESULTS AND DISCUSSIONS

4.1 Structural Analysis

The XRD analysis of SrBi$_{2-x}$Ta$_2$Er$_x$O$_9$ ceramics, with varying concentrations of Er^{3+} (x = 0.00, 0.02, 0.04), are illustrated in Fig. 110.1. The XRD analysis was performed over a 2θ range of 10° to 80°, revealing Bragg reflections that closely correspond to the standard diffraction pattern of SrBi$_2$Ta$_2$O$_9$ as documented in JCPDS card #49-0609. This confirms the formation of a single-phase material without any detectable secondary or unreacted phases, indicating that Er^{3+} ions are fully incorporated into the SBT host lattice without significantly altering its structure.

All samples exhibited the formation of orthorhombic unit cell, corresponding to the space group A21am. The most prominent peak was attributed to the (115) plane of SrBi$_2$Ta$_2$O$_9$, consistent with the bismuth layered structure characterized by n=2.[4]
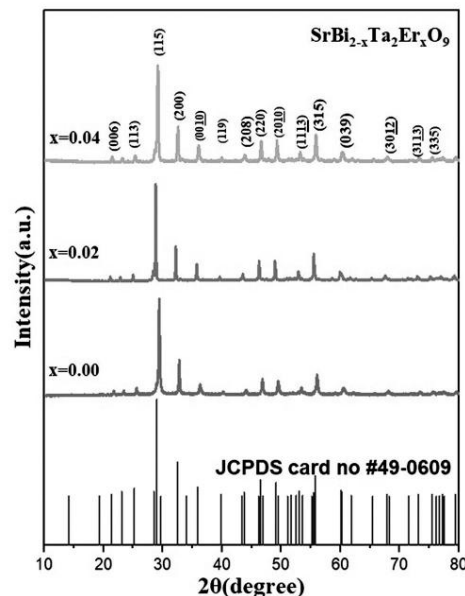

Fig. 110.1 XRD patterns of SrBi$_{2-x}$Ta$_2$Er$_x$O$_9$.

The micro structural characteristics of the sintered ceramic surfaces for SrBi$_{2-x}$Ta$_2$Er$_x$O$_9$ are depicted in Fig. 110.2. The morphology showed grains of varying sizes that are randomly oriented, accompanied by noticeable porosity,
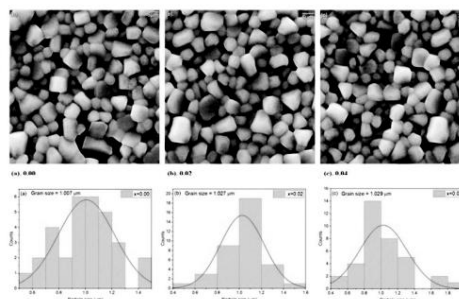

Fig. 110.2 SEM micrographs and histograms of SrBi$_{2-x}$Ta$_2$Er$_x$O$_9$ ceramic

typical of solid-state synthesis methods. As the Er^{3+} content increased, no substantial alterations in grain size were detected.

4.2 Spectral Analysis of Photoluminescence

The Er^{3+}-doped $SrBi_2Ta_2O_9$ ceramics were analyzed for their photoluminescence (PL) properties using an excitation wavelength of 488 nm at room temperature. A prominent green emission was detected within the wavelength (λ) ranges from 536 nm to 556 nm. This strong emission reflects the $^4S_{3/2}$ to $^4I_{15/2}$ and $^2H_{11/2}$ to $^4I_{15/2}$ electronic transitions of Er^{3+} ions.

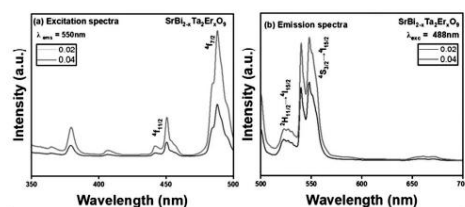**Fig. 110.3** Excitation and Emission Spectra of $SrBi_{2-x}Ta_2Er_xO_9$

▶ 5. CONCLUSION

The study successfully demonstrated the synthesis and characterization of Er^{3+} doped $SrBi_2Ta_2O_9$ ceramics, revealing their structural and photoluminescence properties. The orthorhombic structure was maintained with Er^{3+} doping, while exhibiting strong green emission under 488nm excitation. The optimal doping concentration of x=0.04 provides the most intense luminescence. These findings open up possibilities for further research into rare-earth doped ferroelectric materials for advanced optical applications. Future work could explore different rare-earth dopants, co-doping strategies, or alternative synthesis methods to further enhance the luminescent properties of SBT-based materials.

◀ REFERENCES ▶

1. Shaily, R. and Bokolia, R. (2021). Structural and photoluminescence properties of Er3+ doped SrBi2Nb2O9 ceramics, *Mater Today Proc*, 47:4657–4660.
2. Banwal, A. and Bokolia, R. (2022) Enhanced upconversion luminescence and optical temperature sensing performance in Er3+ doped BaBi2Nb2O9 ferroelectric ceramic," *Ceram Int.* 48(2):2230–2240.
3. Banwal, A. and Bokolia, R. (2021) Effect of Er3+ ion doping on structural, ferroelectric and up/down conversion luminescence in BaBi2Nb2O9 ceramic, *Mater Today Proc*, 47:4692–4695
4. Bokolia, R., Thakur, O. P., Rai, V. K., Sharma, S. K. and Sreenivas, K. (2015) Dielectric, ferroelectric and photoluminescence properties of Er3+ doped Bi4Ti3O12 ferroelectric ceramics, *Ceram Int.* 41(4):6055–6066.